QViT: A Noise-Resilient Quantum-Classical Vision Transformer with Quantum State Tomography for Lung Cancer Classification

BY

Sumaya Mustofa
ID: 242-25-027

This Report Presented in Partial Fulfillment of the Requirements for the Degree of Masters of Science in Computer Science and Engineering

Supervised By

Dr. Md Zahid Hasan
Associate Professor
Department of CSE
Daffodil International University

Co-Supervised By

Dr. Abdus Sattar
Associate Professor
Department of CSE
Daffodil International University

DAFFODIL INTERNATIONAL UNIVERSITY
DHAKA, BANGLADESH
SEPTEMBER 2025

APPROVAL

This Project/Thesis titled **QViT: A Noise-Resilient Quantum-Classical Vision Transformer with Quantum State Tomography for Lung Cancer Classification**, submitted by **Sumaya Mustofa**, ID No: **242-25-027** to the Department of Computer Science and Engineering, Daffodil International University has been accepted as satisfactory for the partial fulfillment of the requirements for the degree of M.Sc. in Computer Science and Engineering and approved as to its style and contents. The presentation has been held on 13-09-2025.

BOARD OF EXAMINERS

Chairman

Dr. S.M Aminul Haque
Professor & Associate Head
Department of Computer Science and Engineering
Faculty of Science & Information Technology
Daffodil International University

Internal Examiner

Ms. Nazmun Nessa Moon
Associate Professor
Department of Computer Science and Engineering
Faculty of Science & Information Technology
Daffodil International University

Internal Examiner

Dr. Md Alamgir Kabir
Assistant Professor
Department of Computer Science and Engineering
Faculty of Science & Information Technology
Daffodil International University

External Examiner

Mr. Sadat Hossain,
Data Scientist,
Risk Management Division,
BRAC Bank Limited

DECLARATION

I hereby declare that this research has been done by me under the supervision of **Dr. Md Zahid Hasan, Associate Professor, Department of CSE,** Daffodil International University. I also declare that neither this project nor any part of this project has been submitted elsewhere for award of any degree or diploma.

Supervised by:

Dr. Md Zahid Hasan
Associate Professor
Department of CSE
Daffodil International University

Co-Supervised by:

Dr. Abdus Sattar
Associate Professor
Department of CSE
Daffodil International University

Submitted by:

Sumaya Mustofa
ID: 242-25-027
Department of CSE
Daffodil International University

©Daffodil International University ii

ACKNOWLEDGEMENT

First, I express my heartfelt thanks and gratitude to Almighty Allah for His divine blessing, which makes it possible to complete the final year project successfully.

I am grateful and wish to express my profound indebtedness to **Dr. Md Zahid Hasan, Associate Professor**, Department of CSE, Daffodil International University, Dhaka, deep knowledge & keen interest in the field of Machine Learning to carry out this project. His endless patience, scholarly guidance, continual encouragement, constant and energetic supervision, constructive criticism, valuable advice, and reading many inferior drafts and correcting them at all stages have made it possible to complete this project.

I would like to express my heartfelt gratitude to **Dr. Sheak Rashed Haider Noori**, **Head of the** Department of CSE, for his kind assistance in completing our project, as well as to the other faculty members and staff of the CSE department at Daffodil International University.

Finally, I must acknowledge with due respect the constant support and patience of my parents.

ABSTRACT

Lung cancer has always been the primary cause of cancer mortality in the world, and the exact identification of its subtypes is still vital in the treatment of patients to enhance their survival. Over the past years, Vision Transformers (ViT) have shown spectacular results in the field of medical image analysis and specifically in detecting and classifying lung cancer. They have not, however, been fully explored in terms of possible integration with quantum computing thus leaving a significant gap to take advantage of quantum advantages of any real clinical significance. To improve the feature learning process, this study proposes a Quantum enhanced Vision Transformer (QViT) framework, in which it incorporates variational quantum circuits (VQC) into attention and feed-forward layers. Basic VQC and Quantum Approximate Optimization Algorithm (QAOA) VQC two-circuit families were tested at two depths resulting in four QViT configurations. The assessments with the help of quantum state tomography (QST) and analysis of noise demonstrated the scalability to deploy on Noisy Intermediate-Scale Quantum (NISQ) devices. This was applied to 3,150 CT images, where the QViT-QAOA-D1 configuration gave 98.52% accuracy, improved to 99.31% with Bayesian hyperparameter optimization without a corresponding increase in circuit resources. Circuits realized in Basic VQC could generate stronger entanglement but had to be deeper-designed whereas QAOA circuits could preserve high-purity states with shallow designs. The results make QViT viable and scalable, hardware-compatible, and make quantum-assisted ViTs an attractive medical AI prospect.

Keywords: Quantum machine learning, Quantum Vision transformer, Variational quantum circuits , Lung cancer classification, Quantum state tomography, NISQ devices

.

TABLE OF CONTENTS

LIST OF FIGURES

LIST OF TABLES

CHAPTER 1
INTRODUCTION

1.1 Introduction

According to WHO, Lung cancer is the number one cause of cancer deaths worldwide with an average of 1.8 deaths per year or out of a total of 25 percent of all cancer deaths. Timely identification of lung cancer subtypes is paramount to improving patient outcomes since survival rates become very different, with 6 percent survival after five years in the case of metastatic lung cancer and a 60 percent survival time range in the event of localized lung cancer reported by American Cancer Society. The classification of lung cancer even in the presence of advanced technologies in the sphere of medical imaging remains under a few challenges associated with cancer heterogeneity (Cellular, histological, molecular diversity) [1], the fine difference in morphological detail between cancer subtypes [2], the poor availability of labelled data because of privacy concerns [3] and the limited radiological expertise [4]. Medical image analysis has traditionally been more adept at benign/malignant classification, but with the need to more finely distinguish between different subtypes, the additional capabilities of new computational approaches could be essential to developing new, advanced feature representation capabilities.

Quantum computing grappling with medical imaging can be regarded as a rising field with a lot of potential in solving clinical problems of the conventional classification of lung cancer. Quantum computing utilizes phenomena in quantum mechanics, including superposition [5] and entanglement [6], to perform exponentially more scalable pattern recognition computations than classical methods, uniquely specialized to pattern recognition [7, 8]. At the same time, Vision Transformers have achieved tremendous progress in the medical imaging domain, outperforming conventional architectures in describing long-range dependencies and spatial relationships, both of which are essential to accurate cancer classification. The convergent point between these two fields offers an ideal situation where quantum-potential attention mechanisms stand a chance of overcoming the computational burden of the classical algorithms, and also the clinical imperative of the requirement of a more accurate diagnostic tool. Quantum variational

circuits (VQC) and their sharing specifications on the Quantum Approximate Optimization Algorithm (QAOA) in particular demonstrated successful performance in feature transformation tasks that can be relevant to medical imaging applications [9, 10], with Vision Transformers being successfully deployed to medical image analysis tools.

1.2 Motivation

Quantum advancements in the cross-section of both quantum machine learning and medical imaging have shown potential but have major deployment barriers. On the quantum side, it was shown that the quantum enhancement of multi-cancer classification can be achieved [11] and that hybrid quantum neural networks can be utilized in skin cancer detection [12]. In medical imaging, Vision Transformer models have demonstrated high scores in terms of accuracy of diagnosis but are relatively computationally demanding, and exhibit lower resolution differentiation ability. Even so, these breakthroughs are somewhat disjointed. Quantum models are usually unverified with reference to clinically relevant data, and are rarely limited by physiologically realistic hardware constraints, whereas medical imaging research has seldom investigated the benefits offered by quantum approaches. Current quantum implementations suffer because they are still based on simulated environments, not real ones, without taking into consideration the deficits of Noisy Intermediate-Scale Quantum (NISQ) devices that are vital to clinical applications [13, 14].These deviations demonstrate the necessity of bringing a coherent framework uniting Vision Transformers and realistic quantum computation to the diagnostic process to increase their accuracy and efficiency.

1.3 Rationale of the Study

Although Vision Transformers and quantum models have demonstrated the potential of medical imaging and quantum models, there is a paucity of literature on the integration of this pair of those to clinically differing lung cancer classes. Earlier work that simulates but does not take into consideration NISQ hardware constraints are either weak in their scope

because it is limited to simulations, or are insufficiently tested on real-world medical datasets thus decreasing their translation potential. Filling this gap is critical in order to create diagnostic systems with the representative capability of Vision Transformers, but with the computational benefits of quantum circuits. This paper is thus justified by the necessity to implement a practical and scalable framework of a quantum-enhanced Vision Transformer (QViT) which could be used to achieve high levels of diagnostic accuracy and at the same time to be compatible with existing quantum hardware to close the gap between theoretical advance and practical relevance.

1.4 Research Questions

- How to integrate the Quantum advantage in Vision Transformer to build a model that can effectively classify lung cancer subtypes?
- How do quantum state tomography (QST) analyses support its quantum contribution?
- What are the options to implement NISQ-compatible circuit design needed to guarantee the useful application of QViT even under the present limits of available hardware?
- What is the noise resiliency level of the proposed model in terms of real NISQ deployment?
- How does QViT compare to state of the art classical Vision Transformers and the available quantum machine learning methods in terms of accuracy, efficiency and scalability?

1.5 Expected Output

This research study is likely to yield quite a number of significant results. First, a new architecture known as Quantum-enhanced Vision Transformer (QViT) will be proposed to show that quantum variational circuits can be better integrated into the attention and feed-forward blocks to enhance feature representations in lung cancer classification. Second,

systematic analysis with a scan representing a clinically relevant case assisted by quantum state tomography (QST) will validate diagnostic performance as well as quantum computational contributions. Third, the work will demonstrate that the NISQ-compatible circuits are feasible and noise can be resisted to demonstrate practical potential to be used on contemporary quantum devices. Last but not least, inter-comparative studies between QViT and classical Vision Transformers as well as with current quantum machine learning approaches will be conducted to ensure that QViT is superior in terms of accuracy, robustness, and computational efficiencies, thus establishing the benchmark in quantum-assisted medical imaging devices of the future.

1.6 Project Management and Finance

Table 1.1: Gantt Chart of the project management.

Task Name	March	April	May	June	July	August
Planning						
Theory Study						
Dataset Collection						
Implementation						
Methodological Implement						
Paper Writing						

This Gantt chart of Table 1.1 displays the time I have spent managing the entire project. I planned the whole project's execution throughout March. At the same time, I did a theoretical study about the components I needed to complete my research and project. I did the dataset collection in April. At the same time, I started to implement the project with another dataset. When dataset collection was done in April, I started to implement the pre-

defined code for April in May with the target dataset. After the targeted dataset implementation, I started to implement the paper with a predefined methodology in June, July and August. Finally, I wrote the paper about the whole experiment in July and August. The research work doesn't get fund from any individuals or organization.

1.7 Report Layout

In Chapter 1, the introduction, motivations, rationale, objectives, and key research inquiries of the study are outlined. In Chapter 2, concise synopses of the literature review are provided. In Chapter 3, the proposed methodology is described in detail. In Chapter 4, the experimental outcomes of the paper are described and examined. The Chapter 5 discusses the sustainability plan, societal and environmental impacts, and ethical considerations. The sixth chapter concludes the present investigation and outlines a strategy for subsequent endeavors.

CHAPTER 2
BACKGROUND

2.1 Preliminaries/Terminologies

New approaches of artificial intelligence and quantum computing have created a paradigm shift in the medical diagnostics field, especially in complicated cases like that of lung cancer classification. Lung cancer, the most frequent cause of cancer deaths, requires precise identification of subtype, wherein the conventional methods tend to fail in dealing with slight variations in medical images. Vision Transformers (ViTs) have become promising deep learning models that are able to capture long-range dependence and focus on global spatial properties and they have already outperformed conventional convolutional models in numerous diagnostic tasks. Similarly, quantum computing, based on superposition and entanglement, makes possible processing of information in exponentially larger feature spaces, and the variational quantum circuit (VQC) and the quantum approximation optimization algorithm (QAOA) are promising directions in near-term applications on Noisy Intermediate-Scale Quantum (NISQ) devices. Moreover, methods like Quantum State Tomography (QST) make it possible to verify real quantum benefit, and thus encompass an extension beyond any classical approximation. In unison, these underlying principles form the root of the proposed Quantum-enhanced Vision Transformer (QViT), which aims to seamlessly combine ViTs with quantum computational functionality in order to reach a strong, noise-resistant, clinically pertinent diagnostic result.

2.2 Related works

Recent works introduced the concept of using Vision Transformers (ViTs) as an alternative to convolutional neural networks (CNNs) in medical image processing, and in many cases achieved superior results to CNNs in terms of classification, segmentation and detection. ViTs can capture longer range dependencies and global spatial relationships compared to

CNNs, which have problems with local receptive fields that hinder them to measure long distance interactions and global spatial dependencies between the objects in the medical image [15, 16]. A formal review of 36 research papers concluded that ViTs outperformed baseline CNN architectures with high accuracy regularly by 253 percent in various diagnostics [17]. ViTs have come to the digital health due to their capability of processing the global context of images. This has worked especially well in segmenting, forecasting, and rebuilding jobs and medical pictures make up almost 90 percent of digital medical data [18] . Applications also include various diseases such as breast cancer, lung disease, skin lesions and in brain tumors whereby ViTs most of the time outperform CNNs [18]. Although this work has made notable progress in this regard, investigations on how quantum computing can be utilized formally embedded into ViT architectures to enhance medical imaging remains unexplored hence this effort would be beneficial in extending the diagnostic functionality of quantum computing to the application domain of medical imaging.

Quantum machine learning (QML) applies the quantum characteristics of superposition and entanglement to deal with problems in high-dimensional and small-sample medical data sets. Oviesi and Tarokh [19] showed this by attaining 56.9 percent emphysema-identification power with the hybrid quantum-classical model when taking into consideration that the given datasets are limited. Similarly, Bilal et al. [11] found an improvement of 6.5% in multi-cancer classification using quantum-inspired optimizers over the traditional learning models. It has also been demonstrated that quantum support vector machines (QSVMs) can minimize the risks of overfitting as compared to quantum neural networks, especially when dealing with imbalanced data [20]. Besides classification, QML has contributed to multimodal learning. Saggi et al. [21] presented a quantum-based multi-omic platform to classify lung cancer and Genç [22] demonstrated that quantum feature maps required fewer parameters by about 30 and reduced the accuracy efficiency. Pauli feature map robustness was also highlighted by Hafidi et al. [23], with the lung cancer classification reaching 92.3% accuracy as opposed to 89.1 for the classical baselines. Systematic reviews, however, point out that among QML studies (n=169 in

2015-2024), few examine models in realistic hardware or noise environments, and thus there is limited evidence on whether they are useful in the real world [24].

Hybrid quantum-classical models remain a revelation as a solution between feature extraction and imaging stability in terms of results in medical imaging. Singh et al. [25] developed a quantum-enhanced GAN to process synthetic data and lung cancer with an accuracy of 99.9%, and 87.3% on clinical data. A quantum-optimized CNN created by Radhika and Sharada [26] attained lung cancer accuracy of 97%, with training time decreasing by 40% device enough. Hussein et al. [12] combined Quantum CNNs with lightweight models and suggested an accuracy of 89.3 percent in skin cancer using 2981 seconds. Gangappa et al. [27] used a hybrid of QML to detect brain tumors, giving a 89 percent Dice coefficient. Research in histopathology has also been a beneficiary such as Mahmood et al. [28] were able to join CNNs and quantum tensor networks to achieve a high of 98.9 and 98.8 percent accuracy with a 25-percent reduction in size. In a comparable approach, Ticku et al. [29] obtained 92.13 percent accuracy on brain tumors using quantum CNN though the cost of computation was high. In spite of these developments, the vast majority of studies are based on simulators and not using actual NISQ devices, and many do not confirm their assertions with quantum state examination. This discrepancy highlights the necessity of clinically focused QML models which facilitate innovation of tomography and noise-sensitive assessment.

Existing near-term Noisy Intermediate-Scale Quantum (NISQ) hardware are limited to simple circuit depths, relatively short qubit coherence times and gate infidelities that can be as high as 0.1-2%. Variational quantum algorithms like QAOA and VQE are noteworthy because they are NISQ-friendly, although, in general, to be successful, they need the depth to be tightly controlled and errors mitigated [10, 9]. Such methods as error extrapolation [30] or stabilizer-based error suppression [31] could yield 15-30 percent more fidelity, but have not been commonly used on medical QML. Quantum state tomography (QST) is becoming an important validation tool to verify authentic quantum computational contributions. Machine learning QST methods have attained reconstruction fidelities over

95 percent with an order of magnitude or larger reduction in the costs of measurements over classical tomography [32; 33]. Quek et al. [34] have further presented transformer based QST methods to perform real-time validation, and demonstrated the applicability of systematic state verifications. Research of medical QML has not yet become as routine as the inclusion of QST or robustness analysis, and it is unclear whether the increase in performance reported is due to a quantum- or preprocessing-based advantage.

2.3 Comparative Analysis and Summary

The comparative analysis and summary below:

Table 2.1: Comparative Analysis of Vision Transformers, Quantum Machine Learning, and Hybrid Models in Medical Imaging.

Authors	**Application**	**Architecture Type**	**Strength**	**Limitations**
Oviesi & Tarokh [19]	Emphysema/COPD	Hybrid (Q-Classical)	Small dataset handling, 0.569 accuracy	Low accuracy, no real-time eval
Singh et al. [25]	Lung Cancer	Hybrid (HWQGAN-CHO)	99.9% accuracy on LC25000	Complex architecture, no NISQ eval
Radhika & Sharada [26]	Lung Cancer	Hybrid (QHO-CNN)	0.97 accuracy, faster training (5.431 hrs)	Still computationally intensive
Bilal et al. [11]	Multi-cancer	Hybrid (Q-GBGWO-ELM)	Multi-cancer detection, 96.98% lung accuracy	Complex optimization, no noise eval
Hussein et al. [12]	Skin Cancer	Hybrid (HQCNN-BiLSTM)	97.7% training, 89.3% test accuracy	Performance gap, no NISQ consideration

Authors	Application	Architecture Type	Strength	Limitations
Gangappa et al. [27]	Brain Tumor	Hybrid (QCNN-CNN)	89% Dice Coefficient, 28% faster inference	Moderate accuracy, no noise analysis
Mahmood et al. [28]	Breast Cancer	Hybrid (CNN-QTN)	98.8% accuracy, parameter reduction	Complex multi-modal approach
Shinde & Pande [35]	Brain Tumor	Hybrid (PQDCNN)	91.52% accuracy, parallel processing	Moderate accuracy, complex architecture
Bilal et al. [36]	Breast Cancer	Hybrid (Q-BGWO-SQSVM)	99% accuracy on CBIS-DDSM	High complexity, no NISQ eval
Scientific [37]	Brain Tumor	Hybrid (QCNN)	99.44% validation accuracy	No real-world testing, no noise eval
Ticku et al. [29]	Brain Tumor	Hybrid (QCNN)	92.13% accuracy, 1.1s vs 64.95s training	Lower accuracy than classical ResNet50
Muniasamy et al. [38]	Brain Tumor	Hybrid (HQC-CNN)	88% accuracy	Lower performance than classical DenseNet121
Awujoola et al. [39]	Breast Cancer	Hybrid (QNN)	Reduced computational time	Classification challenges for malignant cases
Frasca et al. [40]	Melanoma	Hybrid (CNN-QNN)	99.67% precision, 99.35% accuracy	Complex hybrid architecture

Authors	Application	Architecture Type	Strength	Limitations
Rajamohana et al. [41]	Brain Tumor	Hybrid (QGNN)	Novel graph-based approach	Low accuracy (64% training, 52% validation)
Islam et al. [42]	Alzheimer's	Hybrid (CQ-CNN)	97.50% accuracy, 99.99% parameter reduction	Limited to AD, no cancer applications
Saggi et al. [21]	Lung Cancer	Hybrid (QNN)	Multi-omic integration, 0.95 training accuracy	Complex multi-omic requirements
Katı et al. [43]	Deepfake (Not Cancer)	Hybrid (QTL-CaiT)	90% accuracy, transformer integration	Not cancer-related, no medical validation
Balasubramani et al. [44]	Medical Imaging	Hybrid (QANN)	Compression efficiency (71.8-74.1%)	Focus on compression, not diagnosis
Tudisco et al. [20]	Multiple Diseases	Pure Quantum (QNN, QSVM)	QSVM outperforms QNN, handles imbalance	QNN overfitting issues
Genç [22]	Breast Cancer	Hybrid (Quantum Feature Maps)	98.25% accuracy with all features	Feature selection reduces performance
Hafidi et al. [23]	Lung Cancer	Pure Quantum (QSVM)	Perfect classification in 3/6 subsets	Class imbalance challenges

2.4 Scope of the Problem

Identified critical gaps in quantum computing and medical imaging expressions that restrict real-life implementation of quantum-enhanced medical imaging systems are addressed in the literature. In medical image classification, quantum machine learning has proposed realistic future potential in various applications, with accuracy gains reported up to 8-percent over classical algorithms that are due to the quantum resources of parallelism and mapping of high-dimensional features. Nonetheless, existing studies are insufficient in methodological rigor and study-wide meaning, and cannot be replicated in clinical practice. There is a limitation of majority datasets (usually<2,000 images), exclusive reliance on convolutional architectures, restriction to simulated environments thus inabilities to validate solutions in realistic environments using realistic noise levels (0.1-2.0% gate errors).

Although Vision Transformers have enjoyed impressive performance in image analysis and healthcare-related tasks (attaining accuracies of >95% in several studies), the combination of Vision Transformers and quantum machine learning has not yet been attempted. Current research on quantum medical imaging is hampered by the three following challenges: the use of simulated systems, the absence of quantum state tomography to systematically verify states and the absence of quantum-enhanced transformers tailored to medical imaging applications. Lack of quantum state tomography, in-depth noise characterization, and optimization of quantum circuits to NISQ resources cannot facilitate meaningful evaluation of the claims of quantum advantage and hinder the transfer of the theoretical potential in clinically useful medical-AI applications.

2.5 Challenges

The primary limitation in this study derives from the technical and practical limitations to combining quantum computing with medical imaging. First, the current optimals require NISQ devices that have a limited number of qubits with decoherence, short coherence time, and the error rates of the gates can be up to 2%, which negatively affect the performance

of the models. Second, quantum circuit simulations can be very helpful but ultimately cannot compete with real hardware, thus the results may not correspond to clinical implementation. Third, the scale and variability of data can be problematic, since quantum models tend to suffer scalability problems in the form barren plateaus when trained on large datasets. Lastly, to settle the legitimacy of working towards a quantum advantage, we demand the systematic tools like quantum state tomography that are computational demanding and which can conceal multi-qubit correlations. Collectively, these challenges emphasis the challenge of trading diagnostic precision, quantum expressiveness, and feasibility in practice in medical contexts.

CHAPTER 3
RESEARCH METHODOLOGY

3.1 Research Subject and Instrumentation

The research subject of this study is the lung CT image dataset in three categories, namely Normal (1,054), Benign (1,050), and Malignant (1,046). Such balanced categories would help in reliable judgment of the subtype classification. The instrumentation entails the software frameworks and hardware to implement the Quantum-enhanced Vision Transformer (QViT). Data analysis, preprocessing, and model development were done using PyTorch, quantum circuit design and simulation using Qiskit and numerical optimization using JAX. Experiments were performed on a Tesla P100 GPU (16 GB VRAM) on which quantum simulations were modified to meet the requirements of the NISQ era. This installation delivers the practice relevance of information and calculating resources needed in creating and testing the QViT framework.

3.2 Data Collection Procedure/Dataset Utilized

This sample includes chest CT scan images that were successfully captured at the National Institute of Diseases of the Chest and Hospital (NIDCH) in Dhaka, Bangladesh. It has been designed with an intent to support a research project dealing with medical imaging, in particular the classification and early diagnosis of diseases of the lungs through the techniques of artificial intelligence and deep learning. The data set is partitioned into three classifications of diagnosis: 1059 data of malignant, 1054 data of normal (healthy), and 1050 data of benign. All the images were properly labeled and checked by Dr Sabina Akter, MBBS, MD (Radiology & Imaging), Associate Professor and Head of the Department of Radiology and Imaging of NIDCH. The annotations themselves were performed under clinical supervision to make them of high quality, that could be applicable and used in academic/scientific purposes. The reason why data was selected is that it has a proportionate class structure and with the clinical significance of an automated lung cancer classification experiment. Imagery has been collected by reliable sources of clinical

services and has been pre-coded with all labels to offer reliability and repeatability as a research instrument.

Prior to the experiment all images were standardized to normalize data, all the scans were resized to the same dimensions (224 224 pixels) and then normalized to standardize intensities across all the samples to reduce acquisition artefact variability. Such preprocessing steps were important to maintain anatomical information and allow fast training of the proposed QViT model.

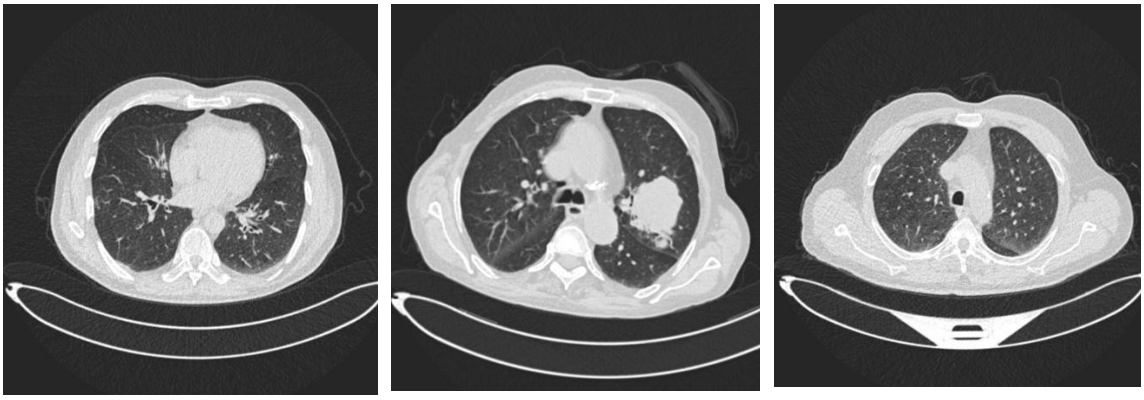

Benign Malignant Normal

Figure 3.1: Images of the three classes from the Lung cancer image dataset.

3.3 Statistical Analysis

The statistical analysis of this study was designed to ensure a rigorous and reliable evaluation of the proposed Quantum-enhanced Vision Transformer (QViT) framework. To perform evaluation, typical classification measures were used, as follows: accuracy, precision, recall, F1-score, area under ROC curve (AUC), and confusion matrix analysis. These measures were selected to reflect the overall predictiveness, as well as ability to discriminate within each of the two classes, malignancy and benignity. To further confirm reliability of the resulting model, stratified k-fold cross-validation and repeat experimental runs using different random seeds were used to yield confidence intervals and minimize stochastic variation in the training.

Comparisons to the best known Vision Transformer models and other quantum machine learning methods were conducted. Statistical significance testing (paired t-tests and Wilcoxon signed-rank tests) was carried out in scenarios where applicable in order to ascertain whether the observed differences in performance were of significant nature or a mere chance effect. Moreover, to demonstrate that the algorithm is robust to realistic NISQ-era constraints, an analysis of noise resilience was performed by testing QViT at different levels of quantum noise (0.0%-2.0%), and results were reported as mean 2 SD across seeds.

This multilayer statistical system gives high validity to the results being both statistically reliable, and meaningful in clinical terms, that the QViT is considerably effective in differentiating lung cancer.

3.4 Proposed Methodology/Applied Mechanism

The flow diagram of figure 3.2 describes the entire process of the proposed Quantum-Enhanced Vision Transformer (QViT) model of lung cancer classification is shown in Figure 3.2. The pipeline begins with collecting data of a patient lung scan CT-scan dataset with three diagnostic groups Benign, Malignant, and Normal. During the preprocessing step, the images are normalized and resized to have consistency and fit in the model. The model generation phase combines traditional patch and positional embedding with a quantum classical transformer encoder with variational quantum circuits to better represent features, before a classifier subnetwork with a classification head to provide the cancer predictive output. The evaluation and optimization has been performed in three phases: (1) performance evaluation, which consists of classification performance assessment of QViT model via accuracy, precision, recall, F1-score, and determination of associated confusion matrices and AUC scores and ROC curves; (2) through Bayesian hyperparameter optimization to tune model parameters, and (3) quantum performance evaluation, which involves quantum state tomography to calculate quantum state fidelity, as well as the noise resiliency analysis to examine robustness under different noise environments.

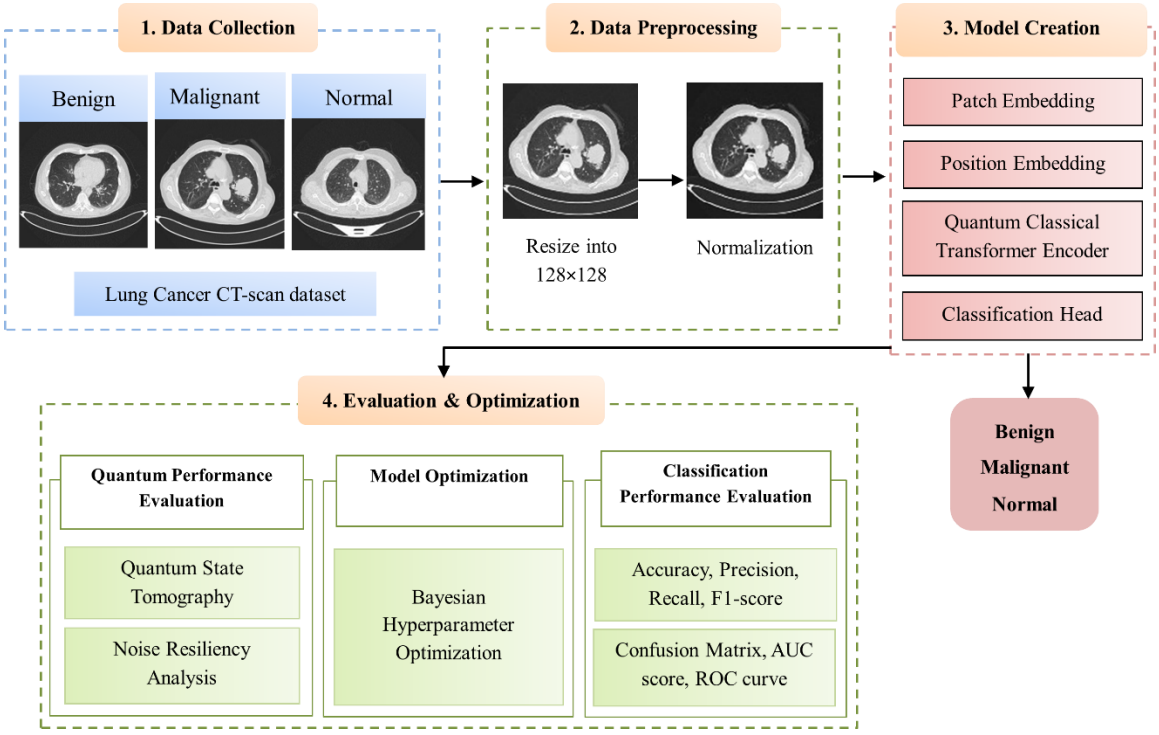

Figure 3.2: Overall methodology of the proposed study consisting four steps: data collection, preprocessing, model creation, and evaluation & optimization.

3.4.1 Data Preprocessing

Lung CT scans usually have variations in contrast, brightness, and acquisition artifacts, thus subtle patterns like lesion boundary and change in tissue densities are difficult to capture. All the images were resized to 224 224 pixels to allow consistency in input to the proposed QViT model, and the intensities were normalized to allow standardization of the range of values within the pixel for computational efficiency. The given preprocessing improves the quality of the received images, minimizes the variability in the data, and saves the vital anatomical details, making the model sufficiently capable of differentiating between benign, malignant, and normal cases.

3.4.2 Hybrid Quantum-Classical Transformer (QViT) Model Architecture

Figure 3.3 demonstrates an entire pipeline of the suggested QViT model. The quantum-classical architecture of QViT model follows a two-level architecture: the external part has

the backbone structure of classical Vision Transformer (ViT), and the inner modules replace the operation of key linear transformations by parameterized quantum circuits. The nature of medical imaging data (high-dimensional and noisy with subtle visual features that require high representational capacity global context modeling) is ideally suited to this formulation.

At a high level, the model begins by partitioning the input image $X \in \mathbb{R}^{B\times H\times W\times C}$ into non-overlapping square patches of size $P \times P$. These are linearly projected into a feature space $\mathbb{R}^d$ via a learnable convolution, forming the token sequence Z_0: $\mathbb{R}^{B\times N\times d}$ where $N = \frac{HW}{P^2}$, B is the batch size, H and W are the height and width of the image, C is the number of channels, d is the hidden embedding dimension. Positional embeddings are added, and the sequence is processed through L number of transformer blocks $TransformerBlock_Q(Z_l)$. Each block enhanced with embedded quantum modules at two bottlenecks: the multi-head self-attention and feed-forward (MLP) modules. The transformer output is passed through a classification head that includes a Global Average Pooling (GAP) operation followed by a dense layer yielding logits over disease categories. This pipeline preserves training stability and compatibility with standard optimizers while infusing quantum expressivity at key points.

3.4.2.1 Classical components of QViT model

In figure 3.3, the classical components of the QViT model are patch embedding, positional encoding, layer normalization, residual connections, classification head illustrated into main QViT pipeline.

Patch Embedding : The patch embedding layer is critical for converting high-dimensional image input into a sequence of low-dimensional embeddings suitable for transformer processing. Specifically, a convolutional projection is applied to each $P \times P$ patch to map it into a d dimensional token:

$$Z_0 = \phi(X) \quad (1)$$

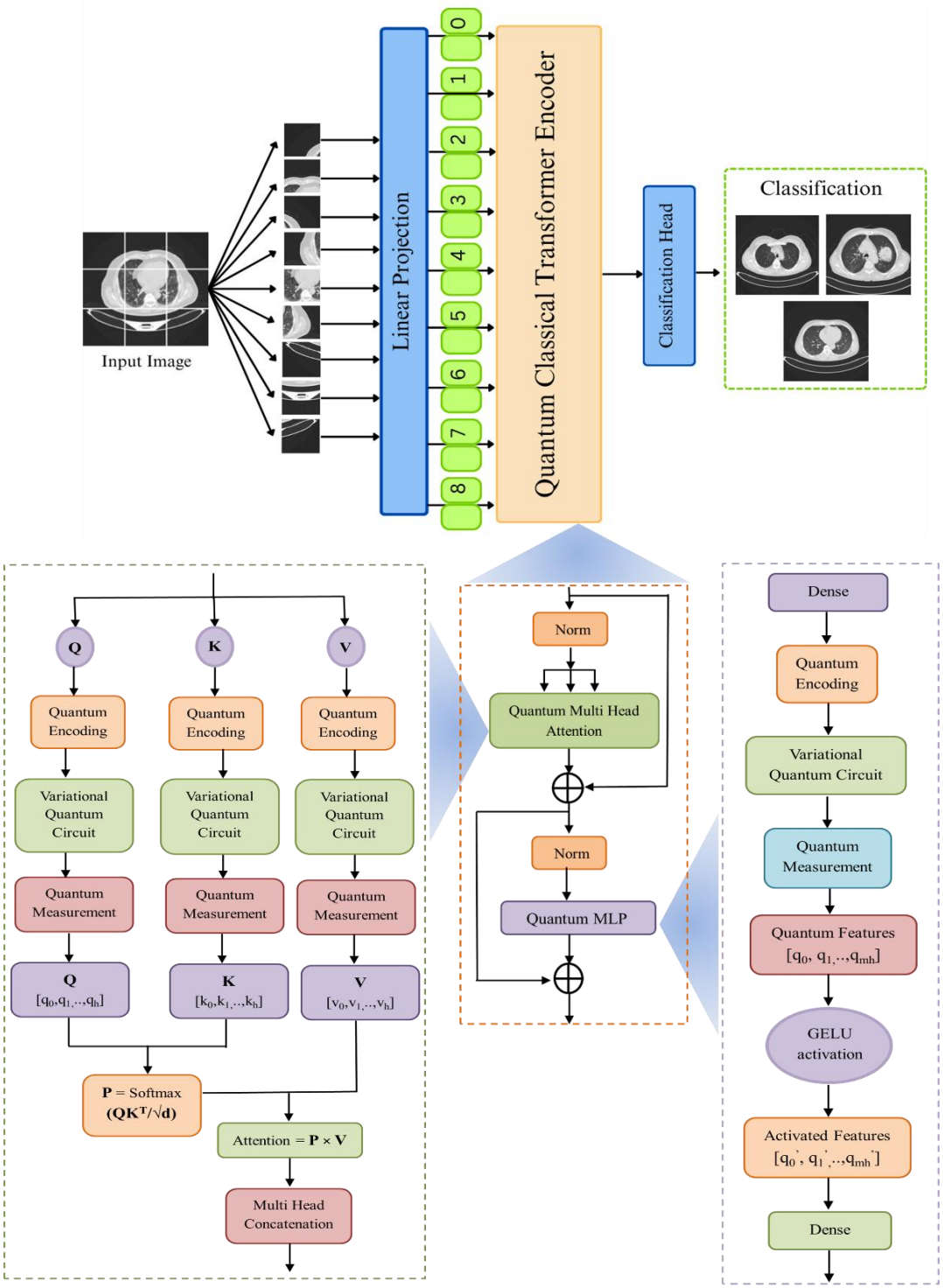

Figure 3.3: Architecture of the proposed QViT model with classical components (patch embedding, positional encoding, layer normalization, residual connections, classification head) and quantum components (quantum multi-head attention, quantum mlp).

Positional Encoding : Transformers lack innate positional understanding. Therefore, positional encoding $P \in \mathbb{R}^{N \times d}$ is added to the patch embeddings to retain spatial order:

$$Z_0 = \phi(X) + P \tag{2}$$

Layer Normalization: Applied before each transformer sub-block. Layer normalization ensures that the input distribution to each module has zero mean and unit variance. This stabilizes training, mitigates internal covariate shift, and promotes better convergence:

$$\hat{Z}_l = LayerNorm(Z_l) \tag{3}$$

Residual Connections: Residual connections or skip connections allow gradients to propagate directly through the network, supporting deeper models and reducing the risk of vanishing gradients:

$$Z_{l+1} = Z_l + f(Z_l) \tag{4}$$

Classification Head: After the sequence has been processed through all transformer layers, a global average pooling (GAP) is applied across the sequence dimension, producing a single vector per sample:

$$\hat{Z} = GAP(Z_L) \tag{5}$$

Finally, a linear dense layer projects the result into the label space:

$$\hat{y} = softmax(W_c^{\hat{Z}} + b_c) \tag{6}$$

This preserves compatibility with classification pipelines while utilizing quantum-enhanced features learned in preceding layers.

3.4.2.2 Quantum components of QViT model

Figure 3.3 further expands into three focused sub-diagrams that clarify how quantum computation is integrated into the transformer encoder. The quantum components of the QViT model are quantum multi-head attention, quantum feed-forward network (quantum MLP in figure 3.3).

(i) Quantum Multi-Head Attention (left panel)

The Quantum Multi-Head Attention module strategically replaces classical linear projections with 12-qubit VQC while preserving the proven attention mechanism framework. Each of the three projection transformations (Query **Q**, Key **K**, Value **V**) employs an independent quantum circuit that processes the full 12-dimensional input features through different configuration of VQC. After quantum processing, the 12-dimensional outputs are reshaped into 2 attention heads of 6 dimensions each, where classical scaled dot-product attention computes token-token relationships through standard softmax operations. The multi-head outputs are then concatenated and processed through a final 12-qubit quantum circuit for output projection.

As depicted in the left panel of figure 3.3, for each attention head $h \in \{1, 2, \ldots., H\}$, three independent VQC circuits generate feature projections:

$$Q = f_{VQC}(X; \theta_Q), \qquad K = f_{VQC}(X; \theta_K), \qquad V = f_{VQC}(X; \theta_V) \tag{7}$$

where f_{VQC} includes a variational circuit acting on n qubits and outputs $d' \leq n$ measurement results. The outputs are then passed through the classical scaled dot-product attention and multi-head concatenation:

$$Attention\ (Q, K, V) = softmax\left(\frac{QK^T}{\sqrt{d'}}\right)V \tag{8}$$

$$MultiHead(Q, K, V) = Concat(Attention^h)\ W^o \tag{9}$$

This step maintains classical softmax dynamics for interpretability and gradient flow while enriching feature representations via quantum transformation. This hybrid design maximizes quantum advantage in the computationally intensive projection phase while maintaining the interpretable attention dynamics that make transformers effective for sequence modeling tasks.

(ii) Quantum Feed-Forward Network (Right Panel)

The Quantum Feed-Forward Network implements a hybrid classical-quantum pipeline that optimizes computational resources through strategic quantum placement. The module begins with classical dense expansion from 12 to 8 dimensions, creating a compressed representation suitable for quantum processing. The 8-dimensional features are then encoded into an 8-qubit VQC . Following quantum measurement, the 8-dimensional quantum features undergo GELU activation before classical dense projection back to 12 dimensions. This architecture intelligently leverages quantum circuits where they provide maximum benefit in the non-linear hidden layer transformation while using classical operations for reliable dimensional manipulation.

The right panel of figure 3.3 represents the integration of quantum computation into the MLP portion of the transformer. This feed-forward transformation follows a three-stage pipeline: classical expansion → quantum enhancement → classical projection.

In classical expansion, feature received 12D and transformed into 8D since mlp_hidden_size parameter was 8.

$$h_{classical} = Dense(x) : \mathbb{R}^{12} \rightarrow \mathbb{R}^{8} \quad (10)$$

In quantum enhancement, classical features 8D features go through encoding, VQC representing by 8 qubits, measurement and transformed into 8D quantum features.

$$h_{quantum} = f_{VQC}(h_{classical}\ \theta;) : \mathbb{R}^{8} \rightarrow \mathbb{R}^{8} \quad (11)$$

Finally, in classical projection, again the 8D quantum features go through GELU activation function and dense layer and transformed into 12D classical features for further processing.

$$y = Dense\left(GELU\left(h_{quantum}\right)\right)\ \mathbb{R}^{8} \rightarrow \mathbb{R}^{12} \quad (12)$$

The compressed quantum processing in MLP uses 8 qubits unlike 12 qubit in attention mechanism. It reduces computational overhead while maintaining sufficient quantum expressivity for feature transformation as the feed-forward network primarily performs

point-wise operations rather than the complex relational modeling required in attention mechanisms.

(iii) Transformer Block (Middle Panel)

The middle panel consolidates these modules into the complete quantum-classical transformer encoder. Each layer includes pre-normalization using LayerNorm, Quantum Multi-Head Attention, Residual Connection, Quantum MLP. The layer output is added to the input via skip connections ensuring stable optimization. This transformer encoder architecture can be stacked L (number of transformer block) times, each with unique circuit parameters

3.4.3 Quantum Circuit Configuration

To formally examine the quantum expressivity and coherence-efficiency trade-offs of the proposed QViT architecture, this paper present two VQC designs, namely the Basic VQC and the QAOA-inspired VQC. Each applied at two depths (constant depths of parameters also known as parameter depth) D1(shallow) and D2(deep). This results in four VQC layouts to produce four QViT versions with different circuit complexities, which allows an orderly analysis of the performance effects.

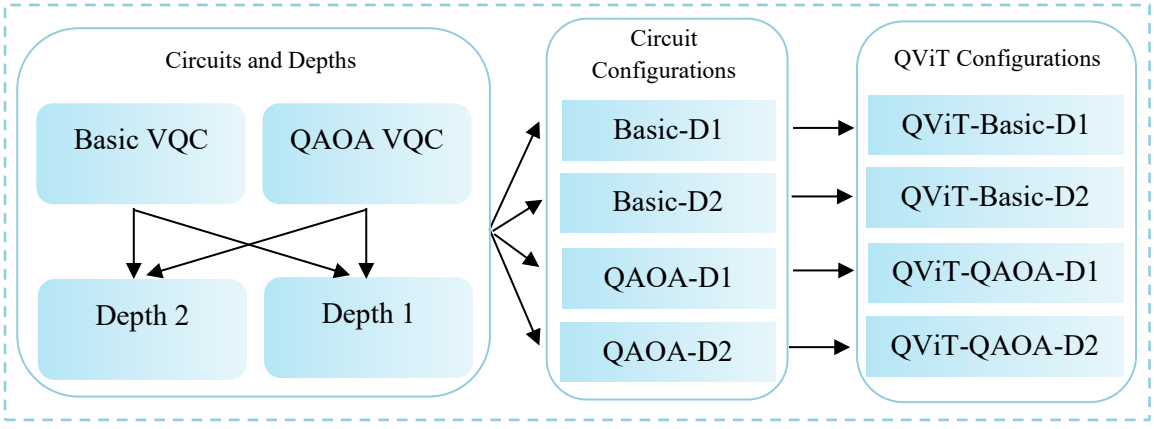

Figure 3.4: Four variational quantum circuit configurations that has been used inside quantum multi head attention (12 qubit) and quantum feed forward network (8 qubit) of QViT model.

The 4 illustrated circuit configurations shown in figure 3.4, that are represented by quantum components of the QViT model and result in 4 distinct QViT architecture. The quantum multi head attention was run with four VQC configurations with 12 qubit (based on the hyperparameter hidden_size) and quantum feed forward network with the four VQC configuration with 8 qubit (based on the hyperparameter MLP_hidden_size). This paper is going to describe in detail 12 qubit quantum circuit configurations together with a brief explanation of 8 qubit quantum circuit configurations.

3.4.3.1 Basic VQC (12 qubit) architecture

The Basic VQC implements a hardware-efficient circuit with full ring connectivity designed to maximize quantum entanglement while maintaining circuit simplicity. The architecture follows a systematic layered approach optimized for universal quantum computation. The complete Basic VQC transformation is expressed as:

$$U_{Basic_{VQC}} = \prod_{l=1}^{L}\left[\prod_{i=0}^{n-1} CNOT(i,(i+1)\ mod\ n)\cdot \otimes_{i=0}^{n-1} RY\left(\theta_i^{(l)}\right)\right]\cdot \otimes_{i=0}^{n-1} RX(x_i) \quad (13)$$

Where, L is number of parameter layers (1 for D1 depth, 2 for D2 depth), n is number of qubits (12 qubits for multi head attention layer and 8 qubits for quantum feed forward network or quantum MLP), x_i is classical input features for qubit i, $\theta_i^{(l)}$ is trainable quantum parameters for layer l and qubit i.

The following 12 qubit Basic VQC has been experimented with two depth configurations:

- **Basic-D1**: Single parameter layer ($L = 1$) with 36 total gates, circuit depth $D = 15$, parameter count: 24 (12 input + 12 trainable)
- **Basic-D2**: Double parameter layer ($L = 2$) with 60 total gates, circuit depth $D = 28$, parameter count: 36 (12 input + 24 trainable)

Similarly, the 8-qubit Basic VQC adopts the same architectural design and circuit depth as the 12-qubit version, with the primary difference being the reduced number of gates due to fewer qubits.

- **Basic-D1:** Single parameter layer ($L = 1$) with 24 total gates, circuit depth $D = 15$, parameter count: 16 (8 input + 8 trainable)
- **Basic-D2**: Double parameter layer ($L = 2$) with 40 total gates, circuit depth $D = 28$, parameter count: 24 (8 input + 16 trainable)

For the QViT-Basic-D1 configuration, the total gate count is 36 for the 12-qubit circuit and 24 for the 8-qubit circuit, resulting in 60 gates within a single transformer block. In comparison, QViT-Basic-D2 consists of 60 gates for the 12-qubit circuit and 40 for the 8-qubit circuit, yielding 100 gates per transformer block. These counts scale linearly with the number of transformer blocks, such that the total gate requirement equals the per-block count multiplied by n.

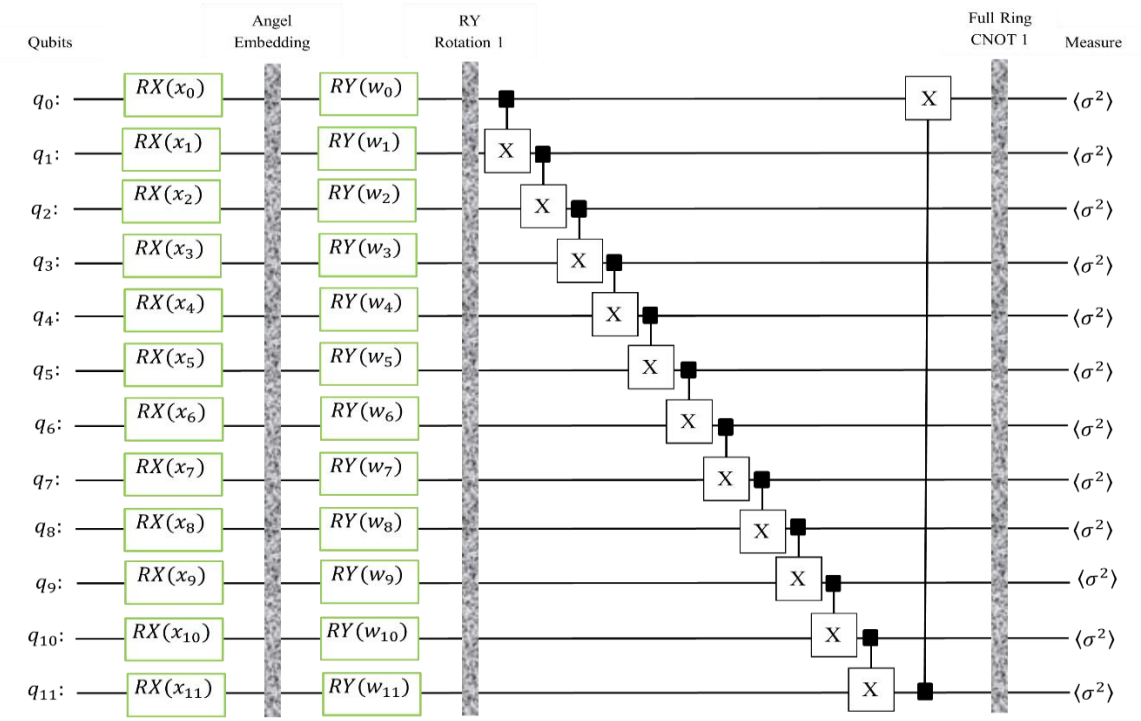

Figure 3.5: Circuit architecture of Basic-D1 (Basic VQC with D1 depth) consists of single RY rotation and single full ring CNOT for 12 qubits.

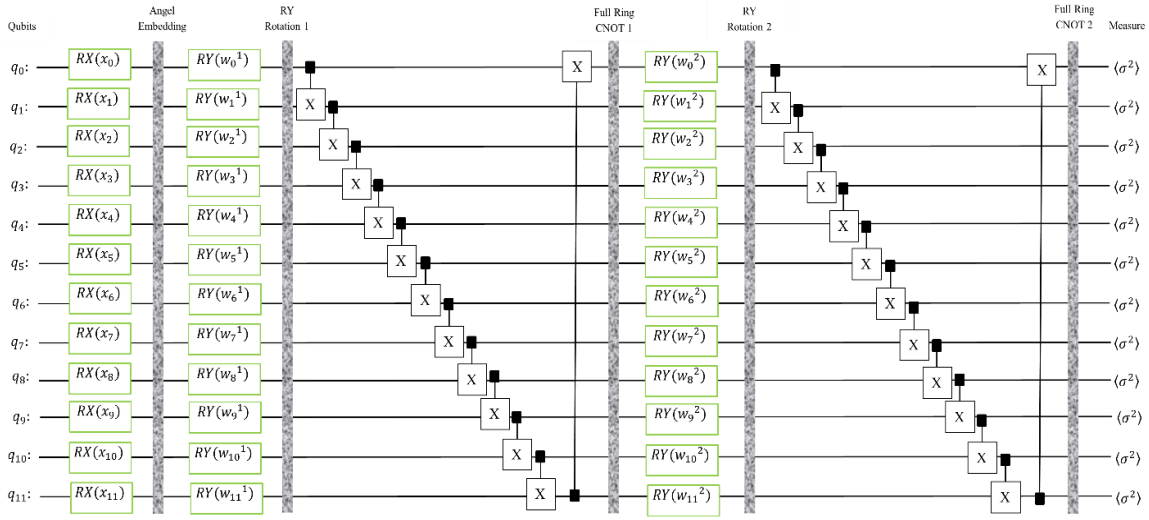

Figure 3.6: Circuit architecture of Basic-D2 (Basic VQC with D2 depth) consists of double RY rotation and double full ring CNOT for 12 qubits.

(i) Components of the Basic VQC circuit

Angle Embedding ($U_{embedding}$) : Classical feature vectors are encoded into quantum amplitudes through single-qubit X-rotations:

$$U_{embedding} = \otimes_{i=0}^{n-1} RX(x_i) = \otimes_{i=0}^{n-1} \begin{bmatrix} cos\left(\frac{x_i}{2}\right) & -i\ sin\left(\frac{x_i}{2}\right) \\ -i\ sin\left(\frac{x_i}{2}\right) & cos\left(\frac{x_i}{2}\right) \end{bmatrix} \quad (14)$$

Where, $x_i \in \mathbb{R}$ is classical input features from neural network, $RX(\theta)$ is Pauli-X rotation gate around X-axis of Bloch sphere. This encoding maps of equation (14) real-valued classical data $x_i \in \mathbb{R}$ to quantum superposition states, creating the initial quantum state $|\Psi_0\rangle = \otimes_{i=0}^{n-1} \left[cos\left(\frac{x_i}{2}\right)|0\rangle \quad -i\ sin\left(\frac{x_i}{2}\right)|1\rangle\right]$.

Parameterized Rotation Layers ($U_{rotation}$) : Trainable quantum parameters are applied through Y-rotations for each layer l :

$$U_{rotation}^{(l)} = \bigotimes_{i=0}^{n-1} RY\left(\theta_i^{(l)}\right) = \bigotimes_{i=0}^{n-1} \begin{bmatrix} cos\left(\frac{\theta_i^{(l)}}{2}\right) & -sin\left(\frac{\theta_i^{(l)}}{2}\right) \\ sin\left(\frac{\theta_i^{(l)}}{2}\right) & cos\left(\frac{\theta_i^{(l)}}{2}\right) \end{bmatrix} \quad (15)$$

Where, $\theta_i^{(l)} \in \mathbb{R}$ are trainable parameters optimized via backpropagation, $RY(\theta)$ is Pauli-Y rotation gate around Y-axis of Bloch sphere, $l \in \{1, 2\}$ layer index (1 layer for D1, 2 layers for D2). These rotations enable variational optimization by rotating qubit states in the Y-Z plane of the Bloch sphere, providing the primary mechanism for quantum machine learning.

Full Ring Entanglement ($U_{entangle}$) : Two-qubit CNOT gates create quantum correlations between adjacent qubits in a ring topology:

$$U_{entangle} = \prod_{i=0}^{n-1} CNOT(i, (i+1)\ mod\ n) \quad (16)$$

where each CNOT gate implements the unitary:

$$CNOT_{i,j} = |0\rangle_i\langle 0| \otimes I_j + |1\rangle_i\langle 1| \otimes \sigma_x^j = \begin{bmatrix} 1 & 0 & 0 & 0 \\ 0 & 1 & 0 & 0 \\ 0 & 0 & 0 & 1 \\ 0 & 0 & 1 & 0 \end{bmatrix} \quad (17)$$

Here, i is control qubit, j target qubit. This creates maximum connectivity with entanglement entropy approaching $\log_2(n)$ for highly entangled states. Creates 12 CNOT connections for 12 qubit (in first layer showed in figure 3.5) : CNOT(0,1), CNOT(1,2), CNOT(2,3), CNOT(3,4), CNOT(4,5), CNOT(5,6), CNOT(6,7), CNOT(7,8), CNOT(8,9), CNOT(9,10), CNOT(10,11), CNOT(11,0). It gets double (24 CNOT) in Basic VQC of D2 architecture (see Figure 3.6).

Quantum Measurement: Observable extraction through Pauli-Z expectation values:

$$y_i = \langle\psi_{final}\,|\,\sigma_z^{(i)}\,|\psi_{final}\rangle = Tr\left(\rho_{final}\,\sigma_z^{(i)}\right),\ \ i = 0, 1, \ldots\ldots, 11 \quad (18)$$

Where, $|\psi_{final}\rangle$ is the final quantum state after all circuit operations, $\sigma_z^{(i)} = \begin{bmatrix} 1 & 0 \\ 0 & -1 \end{bmatrix}$ is the Pauli-Z operator on qubit i, $y_i \in [-1, 1]$ measured expectation value for qubit i, the output is 12-dimensional real vector.

3.4.3.2 QAOA VQC (12 qubit) architecture

The QAOA VQC draws inspiration from quantum optimization algorithms, implementing alternating problem and mixer layers with strategic sparse entanglement designed to balance quantum expressivity with decoherence mitigation. The QAOA transformation follows the alternating problem-mixer paradigm and expressed as:

$$U_{QAOA\_VQC} = \prod_{l=1}^{L} U_{entangle}^{(l)} \cdot \otimes_{i=0}^{n-1} RX\left(\theta_i^{(l)}\right) \cdot \otimes_{i=0}^{n-1} RZ\left(x_i + \theta_i^{(l)}\right) \quad (19)$$

Where, $U_{entangle}^{(l)}$ is sparse entanglement (only applied in first layer).

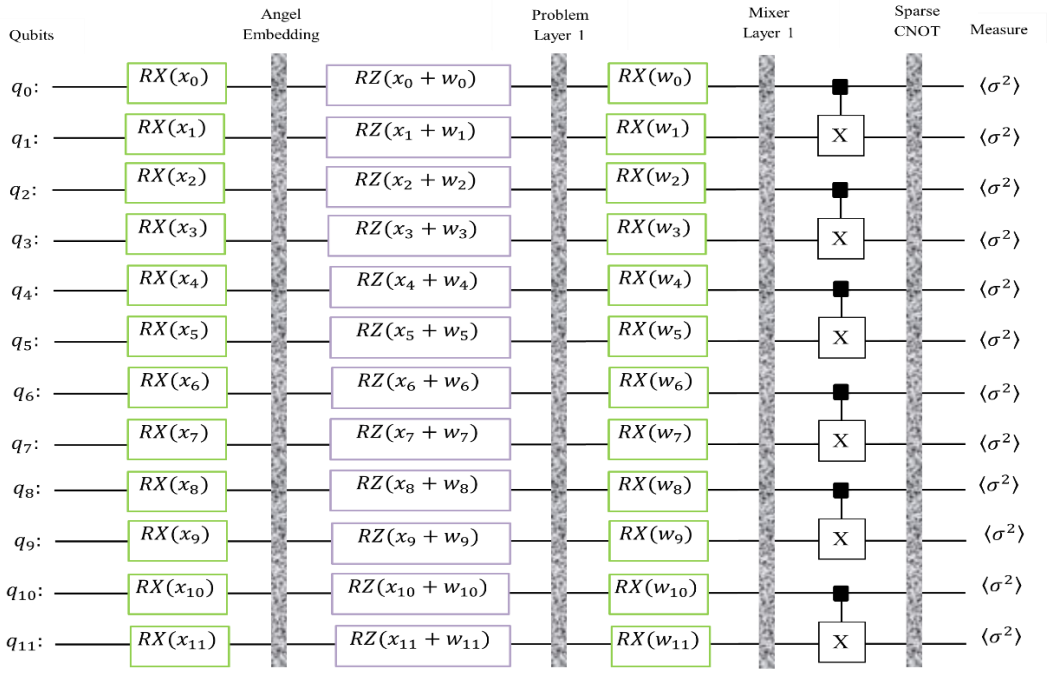

Figure 3.7: Circuit architecture of QAOA-D1 (QAOA VQC with D1 depth) consists of single problem layer, single mixer layer and single sparse CNOT.

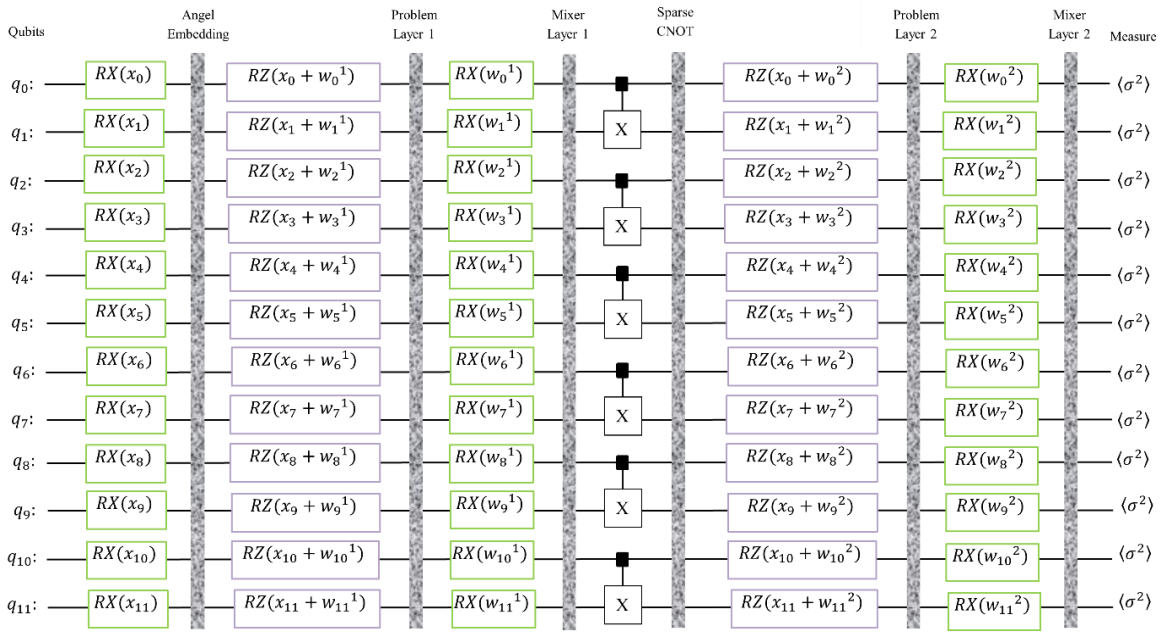

Figure 3.8: Circuit architecture of QAOA-D2 (QAOA VQC with D2 depth) consists of single problem layer, single mixer layer and single sparse CNOT.

The following 12 qubit QAOA VQC has been experimented with two depth configurations:

- **QAOA-D1**: Single layer ($L = 1$) with 42 total gates, circuit depth $D = 5$, parameter count: 18 (12 input + 6 trainable)
- **QAOA-D2**: Double layer ($L = 2$) with 66 total gates, circuit depth $D = 7$, parameter count: 24 (12 input + 12 trainable)

Similarly, the 8-qubit QAOA VQC adopts the same architectural design and circuit depth as the 12-qubit version, with the primary difference being the reduced number of gates due to fewer qubits.

- **QAOA-D1**: Single layer ($L = 1$) with 28 total gates, circuit depth $D = 5$, parameter count: 12 (8 input + 4 trainable)
- **QAOA-D2**: Double layer ($L = 2$) with 44 total gates, circuit depth $D = 7$, parameter count: 16 (8 input + 8 trainable)

For the QViT-QAOA-D1 configuration, the total gate count is 42 for the 12-qubit circuit and 28 for the 8-qubit circuit, resulting in 70 gates within a single transformer block. In comparison, QViT-QAOA-D2 consists of 66 gates for the 12-qubit circuit and 44 for the 8-qubit circuit, yielding 110 gates per transformer block. These counts scale linearly with the number of transformer blocks, such that the total gate requirement equals the per-block count multiplied by n.

(i) Components of the QAOA VQC circuit

Angle Embedding ($U_{embedding}$) : Identical to Basic VQC using $RX(x_i)$ rotations for classical-to-quantum state preparation.

Problem Layer ($U_{problem}$) : Direct encoding of data-parameter coupling through Z-rotations:

$$U_{problem}^{(l)} = \otimes_{i=0}^{n-1} RZ\left(x_i + \theta_i^{(l)}\right) = \otimes_{i=0}^{n-1} \begin{bmatrix} e^{-i\left(x_i + \frac{\theta_i^{(l)}}{2}\right)} & 0 \\ 0 & e^{i\left(x_i + \frac{\theta_i^{(l)}}{2}\right)} \end{bmatrix} \quad (20)$$

Where, $\left(x_i + \theta_i^{(l)}\right)$ is direct data-parameter coupling that is key QAOA innovation, $RZ(\phi)$ is Pauli-Z rotation gate around Z-axis of Bloch sphere, $\theta_i^{(l)}$ is trainable parameter in problem layer. The key innovation of QAOA problem layer lies in the additive coupling $\left(x_i + \theta_i^{(l)}\right)$, which directly integrates classical input data with trainable quantum parameters, enabling efficient hybrid classical-quantum information processing.

Mixer Layer (U_{mixer}) : Quantum mixing through X-rotations:

$$U_{mixer}^{(l)} = \otimes_{i=0}^{n-1} RX\left(\theta_i^{(l)}\right) = \otimes_{i=0}^{n-1} \begin{bmatrix} \cos\left(\frac{\theta_i^{(l)}}{2}\right) & -i\sin\left(\frac{\theta_i^{(l)}}{2}\right) \\ -i\sin\left(\frac{\theta_i^{(l)}}{2}\right) & \cos\left(\frac{\theta_i^{(l)}}{2}\right) \end{bmatrix} \quad (21)$$

Where, $RX(\theta)$ is Pauli-X rotation for quantum state mixing. This layer provides quantum "mixing" that enables exploration of the quantum state space while preserving the problem structure encoded in the preceding layer.

Sparse Entanglement ($U_{entangle}$) : Pair-wise CNOT gates with reduced connectivity applied only in the first layer where I is denoted as identity (no entanglement in subsequent layers):

$$U_{entangle}^{(l)} = \prod_{k=0}^{(n/2)} CNOT(2k, 2k+1), \qquad U_{entangle}^{(l>1)} = I \tag{22}$$

This creates entanglement pairs for 12 qubit (only in first layer and no CNOT for QAOA-D2): CNOT(0,1), CNOT(2,3), CNOT(4,5), CNOT(6,7), CNOT(8,9), CNOT(10,11) providing 50% reduction in two-qubit gates compared to basic VQC while maintaining sufficient quantum correlations (see figure 3.7, figure 3.8).

Quantum Measurement: Identical as basic VQC measurements of equation (18).

3.4.4 Quantum State Tomography

Quantum State Tomography (QST) facility allows a controlled measurement of quantum states in the QViT architecture using Pauli measurement protocols. In this work, QST was applied on two circuit scales based on the heterogeneous model implementation: 12-qubit variational quantum circuit (VQC) of the quantum multi-head attention and 8-qubit VQC of the quantum feed-forward network with four variations each. This two-scale structure involved two tiers of QST analysis. To gain strict validation of quantum characteristics, the experiment was performed in noiseless and 1 % noise cases over all circuit designs.

Full-system quantum state tomography becomes computationally intractable for large qubit systems (for 12 qubit $4^{12} \approx 16M$ and for 8 qubit $4^8 \approx 65K$) due to exponential scaling in measurement requirements and reconstruction complexity. To address this limitation, quantum circuits were partitioned into manageable 4-qubit subsystems: 8-qubit systems into two subsystems and 12-qubit systems into three subsystems. Each subsystem

underwent independent tomographic reconstruction using 4^4 = 256 Pauli measurements and maximum likelihood estimation. System-level quantum metrics (fidelity, entropy, entanglement, purity, trace distance, QFI) were obtained by averaging across all subsystems within each configuration. This approach balances computational feasibility with representative quantum state characterization, though it may mask subsystem-level performance variations.

For an 4-qubit quantum subsystem, the quantum state $|\psi\rangle$ can be fully characterized through its expectation values over the complete Pauli operator basis:

$$\langle P\rangle = \langle\psi \mid P \mid\psi\rangle \quad for\ all\ P \in P_4 \tag{23}$$

3.4.4.1 Quantum Information Metrics

Fidelity: Fidelity quantifies the overlap between true and reconstructed quantum states, providing a direct measure of tomographic reconstruction quality. With perfect reconstruction yielding F = 1 and orthogonal states giving F = 0. In quantum machine learning contexts, higher fidelity indicates better preservation of quantum information during circuit execution and more accurate state preparation. Mathematically,

$$F(\rho,\sigma) = Tr\left(\sqrt{\sqrt{\rho}\,\sigma\sqrt{\rho}}\right)^2 \tag{24}$$

Where, ρ is true density matrix and σ is reconstructed density matrix.

Von Neumann Entropy: Measures the quantum state's mixedness and information content through eigenvalue distribution. Pure states (single non-zero eigenvalue) yield S = 0, while maximally mixed states approach $log_2(d)$ where d is the Hilbert space dimension. Higher entropy values indicate greater exploration of quantum state space, which can enhance expressivity in quantum neural networks but may reduce coherence. Mathematically,

$$S(\rho) = -Tr(\rho\ log_2\ \rho) = -\sum_i \lambda_i \log_2 \lambda_i \tag{25}$$

Where, ρ is density matrix with eigendecomposition, λ_i is i[th] eigenvalue of ρ.

Entanglement Entropy: Quantifies quantum correlations by analyzing the reduced density matrix $\rho A = Tr_B(\rho AB)$ of one subsystem. This metric captures non-classical correlations essential for quantum computational advantage. Higher entanglement entropy indicates stronger quantum correlations that can enable parallel quantum processing but may be more susceptible to decoherence in NISQ devices.:

$$S_{entanglement}(\rho AB) = -Tr(\rho A \log_2 \rho A) \quad (26)$$

$$\rho A = Tr_B(\rho AB) \quad (27)$$

Where, ρA is the reduced density matrix of subsystem A only, ρAB is density matrix of the combined bipartite system , Tr_B is partial trace over subsystem B.

Purity: Indicates the quantum state's proximity to a pure state through the sum of squared eigenvalues. Pure states achieve Purity = 1, while maximally mixed states approach Purity = 1/d. High purity suggests minimal decoherence and strong quantum coherence preservation, which benefits NISQ compatibility but may limit computational expressivity in quantum machine learning applications.

$$Purity(\rho) = Tr(\rho^2) = \sum_i {\lambda_i}^2 \quad (28)$$

Where, ρ is density matrix and λ_i is eigenvalues.

Trace Distance: Measures the statistical distinguishability between quantum states, serving as a reconstruction error metric in QST. Lower trace distances indicate superior tomographic fidelity and more reliable quantum state characterization. This metric is particularly important for validating the accuracy of quantum state tomography protocols and comparing reconstruction quality across different architectures.

$$D(\rho, \sigma) = \frac{1}{2} Tr(|\rho - \sigma|) = \frac{1}{2} \sum_i |\lambda_i(\rho - \sigma)| \quad (29)$$

Where, $|\rho - \sigma|$ is absolute difference between true and reconstructed matrix (Hermitian), $\lambda_i(M)$ is ith eigenvalue of any matrix M.

Quantum Fisher Information (QFI): Quantifies the quantum state's sensitivity to parameter changes through the generator Hamiltonian H, determining precision limits for quantum parameter estimation. Non-zero QFI enables quantum-enhanced sensing applications, while QFI = 0 indicates the state provides no advantage for parameter estimation tasks. This metric helps distinguish between quantum states optimized for computation versus sensing applications.

$$F_Q(\rho, H) = 2\sum_{i,j} \frac{(\lambda_i - \lambda_j)^2}{\lambda_i + \lambda_j} |\langle i| H |j\rangle|^2 \quad (30)$$

Where, H is Generator Hamiltonian (Hermitian operator defining parameter dependence), $\langle i|, |j\rangle$ is eigenvectors of ρ corresponding to eigenvalues λ_i and λ_j, $\langle i| H |j\rangle$ is matrix element of H between eigenstates.

Multi System Averaging: All metrics employ arithmetic averaging across N subsystems, providing system-level characterization while potentially masking subsystem-level variations in quantum state quality.

$$Metric_{system} = \frac{1}{N}\sum_{i=1}^{N} Metric(\rho_i) \quad (31)$$

Where, N is number of subsystems (2 for 8-qubit, 3 for 12-qubit), ρ_i is density matrix of i-th subsystem, metric refers to fidelity, entropy, purity, trace distance etc.

3.4.5 Bayesian Hyperparameter Optimization

Bayesian optimization offers a principled method to efficiently search hyperparameters using probabilistic surrogate models to make informed decisions in easily exploring a multi-dimensional parameter space with low computing expense. The optimization algorithm compensates the exploration of the unknown areas and exploitation of the local high-performing areas using the Expected Improvement acquisition function, thus performing an optimal mode of systematic search. Seven hyperparameters are considered most critical that are systematically optimized with constrained parameter ranges in this

work: patch size, hidden dimensions, attention heads, transformer depth, MLP capacity, learning rate, and regularization strength or dropout shown in table 3.1.

Table 3.1: Optimization Strategy and Parameter Space.

Parameter Name	**Parameter Space**
Patch size	[32, 64, 128]
Hidden size	[4, 8, 12, 16]
Number of heads	[2, 4, 6, 8]
Transformer blocks	[1, 2, 4, 8,12]
MLP hidden size	[4, 8, 12, 16, 20, 24]
Learning rate	[1e-4 - 1e-2, logarithmic range]
Dropout rate	[0.0, 0.1, 0.2, 0.3, 0.4, 0.5]

The framework ensures quantum circuit efficiency and NISQ hardware compatibility while maximizing diagnostic performance through iterative refinement of the quantum-classical hybrid architecture configuration.

Bayesian optimization models the objective function $f(X)$ using a Gaussian Process prior where $\mu(X)$ is the mean function and $k(X, X')$ is the covariance kernel function:

$$f(X) \sim \mathcal{GP}(\mu(X), k(X, X')) \tag{32}$$

The Expected Improvement acquisition function guides hyperparameter selection:

$$EI(X) = \mathbb{E}[\max(f(X) - f(X^+), 0)] \tag{33}$$

Where, $f(X^+)$ represents the current best observed value, balancing exploration of uncertain regions with exploitation of promising areas.

The Parameter Space Optimization seeks to maximize diagnostic performance $f(X)$ over the hyperparameter space $X \in \mathcal{X}$:

$$X^* = \underset{X \in \mathcal{X}}{argmax}\, f(X) \tag{34}$$

Where $\mathcal{X}$ represents the constrained parameter space ensuring quantum circuit compatibility and computational feasibility.

Sequential optimization terminates when the acquisition function improvement falls below threshold ϵ maximum iterations T are reached. This is the convergence criteria for Bayesian Optimization. Mathematically,

$$|EI(X_{t+1}) - EI(X_t)| < \epsilon \quad or \;\; t \geq T \tag{35}$$

3.4.6 Noise Resilience Analysis

This paper will offer a strict noise resilience test to estimate the reliability of QViT models proposed and determine how they will behave at NISQ operational levels. The performance results are plotted at seven noise levels (0.0% to 2.0%) under realistic conditions of working NISQ devices such as those during ideal circumstances to restrictive but realistic hardware settings. Each of the noise levels is related to the error rates in gates of current quantum processors: IBM Quantum 0.1-1.0% gate errors [45], Google Sycamore 0.1-0.5% [46] , and IonQ systems 0.1-2.0% [47], making these models relevant to experiments in real quantum hardware deployment.

To make this noise resilience analysis more inclusive this is study incorporated seed base analysis, using seed 42, 142, 242. Triple-seed assessment (n=3) will provide statistical robustness to the analysis of stochastic quantum error processes to provide confidence intervals on the performance metrics under noisy conditions and take into consideration the probabilistic nature of quantum decoherence and measurement uncertainty inherent in NISQ devices. The analysis of performance variations will be done within acceptable clinical diagnostic tolerances (±2-3% accuracy) to confirm that the quantum advantage would not be obsoleted by hardware limitations such as NISQ systems potentially falling within clinical realistic conditions deployment and practical viability of the medical imaging application.

3.4.7 Classification Performance Assessment

The classification performance of the proposed QViT model on the lung cancer dataset was comprehensively evaluated using multiple metrics, including accuracy, precision, recall, F1-score, confusion matrix analysis, AUC score, and ROC curve assessment.

$$Accuracy = \frac{TP + TN}{TP + FP + TN + FN} \tag{36}$$

$$Precision = \frac{TP}{TP+FP} \tag{37}$$

$$Recall = \frac{TP}{TP+FN} \tag{38}$$

$$F1 - score = \frac{2 \times Precision \times Recall}{Precision + Reacll} \tag{39}$$

3.5 Implementation Requirements

The simulations on all the variants of the QViT model were performed on PyTorch and linked to Qiskit and JAX to simulate quantum logical networks and to perform numerical computations, respectively. It was trained on Kaggle 2 Tesla P100 (16 GB VRAM) with CUDA support. The models used standard precision training to make them compatible with available computation facilities.

CHAPTER 4
EXPERIMENTAL RESULTS AND DISCUSSION

4.1 Experimental Setup

Lung cancer CT scan images were resized to 224 × 224 pixels and normalized to [0,1] prior to training. The dataset of 3,150 CT images was divided into 70% training (2,205 images), 15% validation (472 images), and 15% testing (473 images) to ensure balanced evaluation across classes. The proposed QViT model was configured with initial training (pre-optimization hyperparameter setup) patch size = 128, hidden size = 12, number of heads = 2, one transformer block, MLP hidden size = 8, dropout rate = 0.1, and a warmup cosine decay learning rate schedule. Optimization was carried out using the Adam optimizer. Noise resilience was further assessed by simulating quantum error rates from 0.0% to 2.0% under NISQ constraints.

4.2 Experimental Results & Analysis

This subsection presents experimental results analyzing the classification performance of the proposed QViT model on the lung cancer dataset and the quantum performance characteristics of the underlying circuit architectures.

4.2.1 Classification Performance Analysis of QViT model

Table 4.1 includes results of classification of the QViT model variations on the lung cancer dataset. Among the models, QViT-QAOA-D1 has the second highest accuracy of 98.52 percent and relatively low training time of 674.73 seconds. Therefore, QViT-QAOA-D1 is highly efficient and diagnostic. Comparatively, QViT-QAOA-D2 had 98.85% accuracy, but it takes much longer time to train which is 1197.60 seconds, implying that a deeper circuit is more costly in terms of computation. The Basic VQC variations show slightly reduced performance, wherein, QViT-Basic-D2 returns an accuracy of 97.04% in 861.54 seconds, and QViT-Basic-D1 the lowest at 96.83% accuracy but converges the fastest at 533.54 seconds. These findings indicate the superiority of QAOA-based arrangements that

show better performance in diagnosis accuracy as compared to Basic VQC, with desirable trade-offs between the execution time and accuracy.

Table 4.1. Classification performance analysis of the QViT model configurations on Lung Cancer dataset.

Variant	Accuracy	Number of Parameters	Training Time
QViT-Basic-D1	96.83 %	196,787	533.54 seconds
QViT-Basic-D2	97.04 %	196,787	861.54 seconds
QViT-QAOA-D1	98.52 %	196,987	674.73 seconds.
QViT-QAOA-D2	98.85 %	196,987	1197.60 seconds

Comparison of the training and validation dynamics on the four QViT models are illustrated in figure 4.1. The QViT-QAOA-D1 and QViT-QAOA-D2 models perform consistently and basically follow a similar trend as reported in QViT-D1. Their convergence is less volatile and the loss is reduced much faster with accuracy stabilizing at around the same point as QViT-D1 at 15-20 epochs. Their validation curves demonstrate little fluctuation with a strong generalization. Figure 4.1 (a) compares optimizations during Basic VQC models (QViT-Basic-D1 and QViT-Basic-D2) to sky rocket loss and accuracy after early convergence with the optimizations of Deep VQC models (QViT-Deep-D1 and QViT-Deep-D2). QViT-Basic-D2 has lower convergence speed but higher performance variance and, conversely, QViT-Basic-D1 is a highly unstable, slow-converging algorithm. These variations highlight that QAOA problem-encoded solutions exhibit greater covered performance because of their enhanced consistency with a greater chance of clinical utility than Basic VQC hardware-efficient solutions.

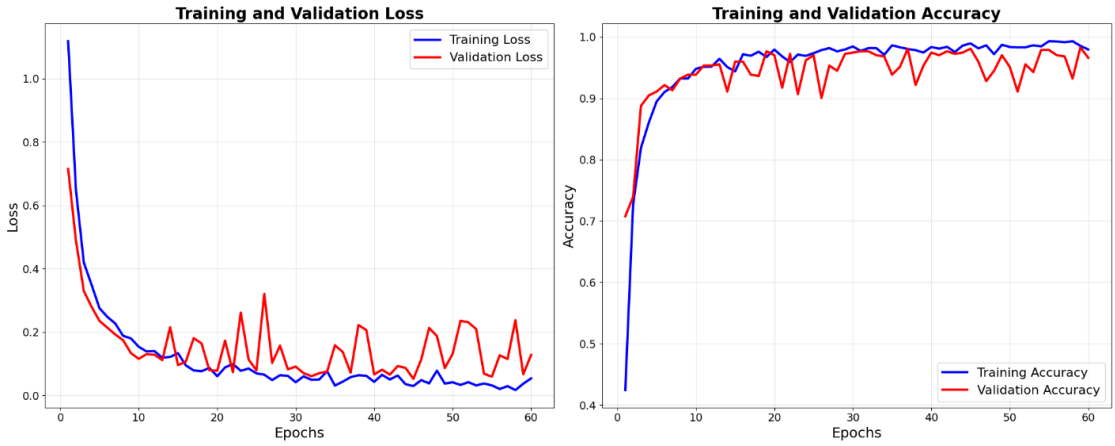

(a) QViT-Basic-D1

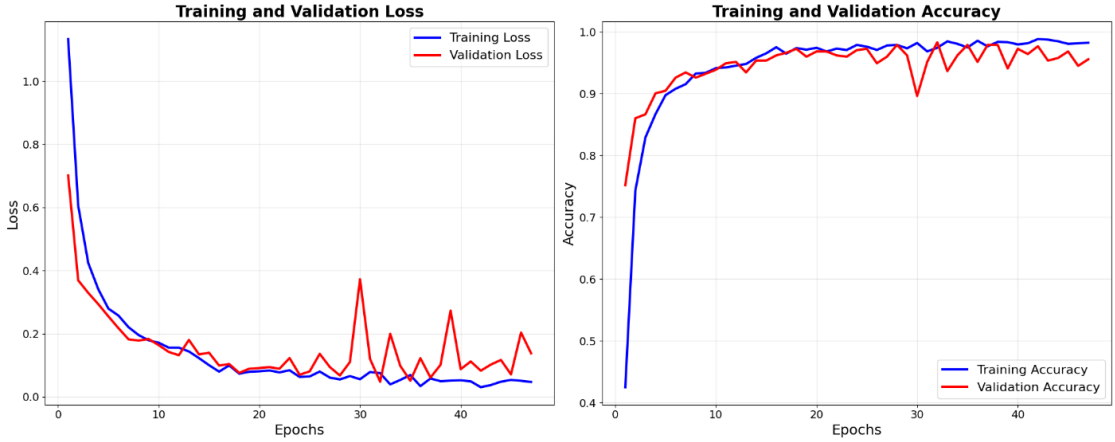

(b) QViT-Basic-D2

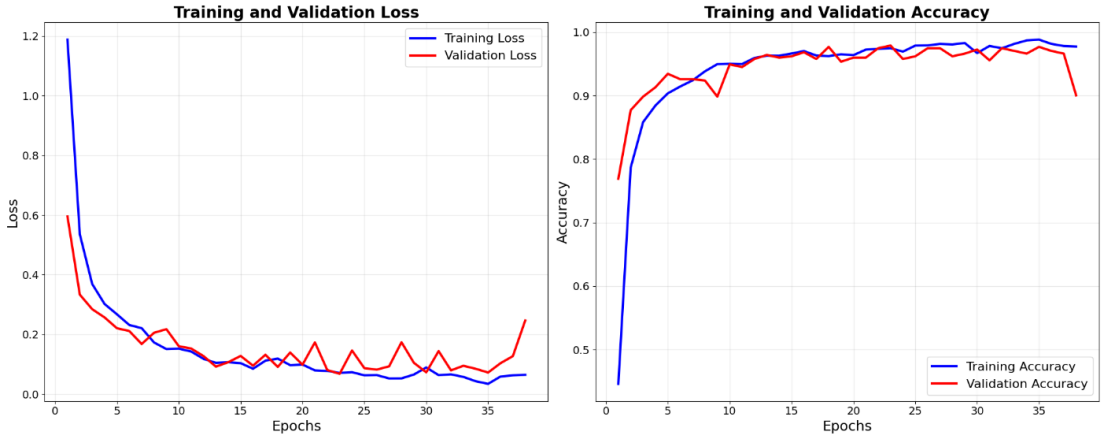

(c) QViT-QAOA-D1

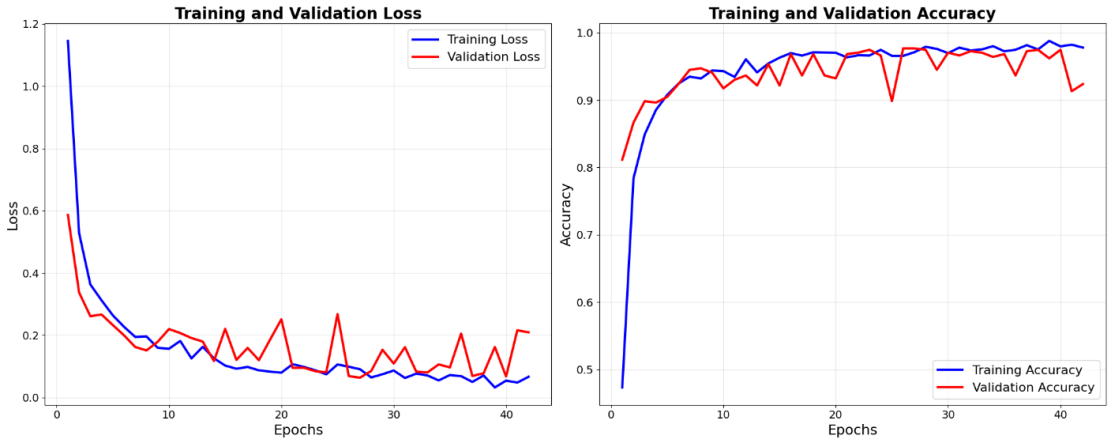

(d) QViT-QAOA-D2

Figure 4.1. The training and validation loss curve (left) and training and validation accuracy curve (right) of four QViT configuration (a) QViT-Basic-D1, (b) QViT-Basic-D2, (c) (d) QViT-QAOA-D1, (d) QViT-QAOA-D2 .

The confusion matrices in Figure 4.2 starkly define the fact that the QAOA-based models are superior to Basic VQC models. ViT-QAOA-D2 performs better and correctly classifies all normal cases (158/158) and misclassifies only a single benign and 6 malignant cases as benign. QViT-QAOA-D1 shows balanced performance with a small number (3) of benign cases falsely identified as malignant and (4) of malignant cases falsely identified as benign, plus a perfect recognition of normal cases (157/158). Comparatively, QViT-Basic-D1 shows more errors, including 8 benign cases misclassified as malignant; however, QViT-Basic-D2 clearly show weaker benign labeling with 7 cases transformed as malignant. Most importantly, all versions show excellent specificity to healthy tissue, with only one misclassification over the Basic variants. The above results together with the findings in the previous paragraphs make it clear that QAOA-based parameterizations have consistently offered the most reliable and clinically feasible estimations as opposed to those of the basic parameters.

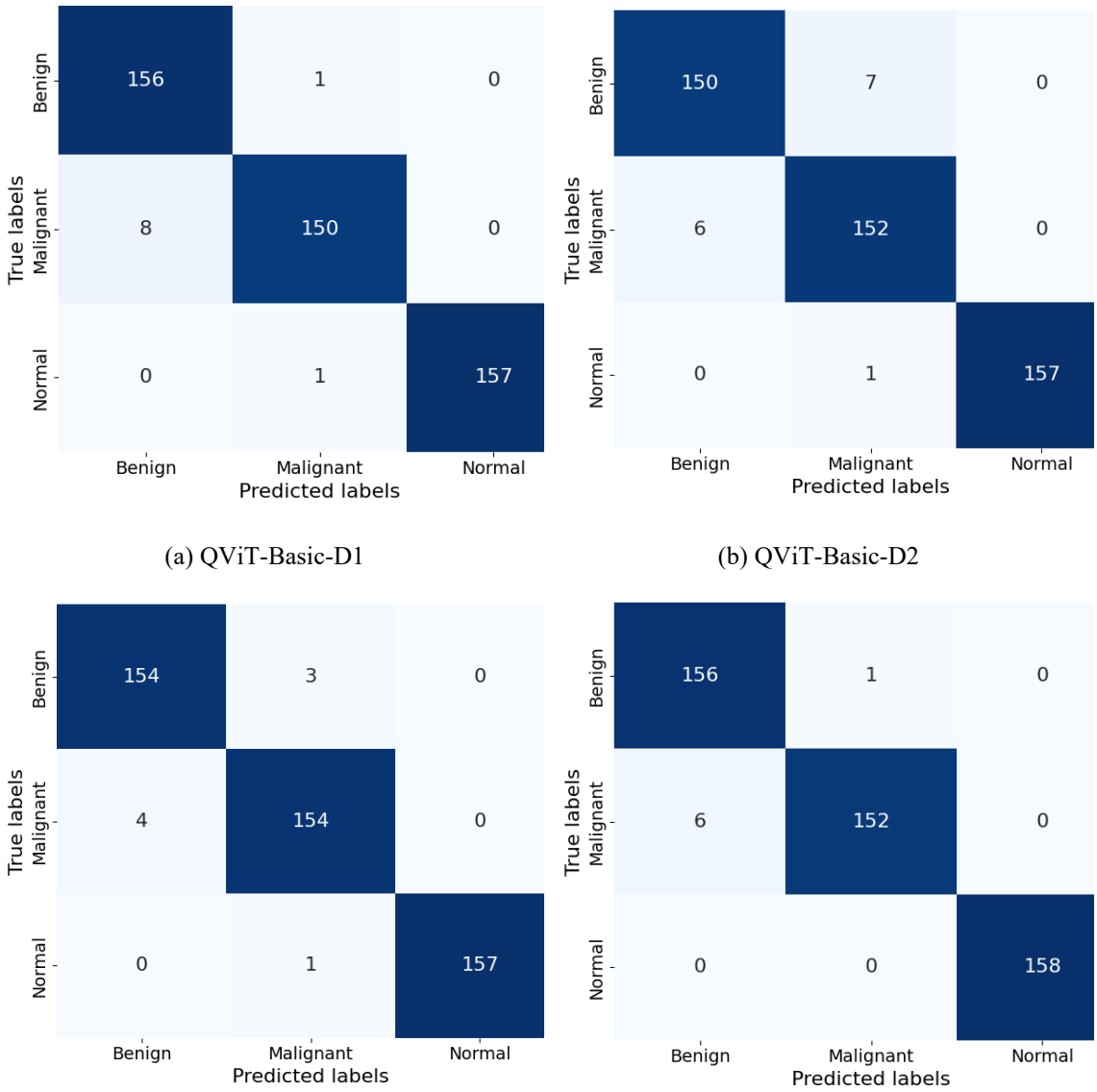

(a) QViT-Basic-D1

(b) QViT-Basic-D2

(c) QViT-QAOA-D1

(d) QViT-QAOA-D2

Figure 4.2. The Confusion matrices of four QViT configuration (a) QViT-Basic-D1, (b) QViT-Basic-D2, (c) (d) QViT-QAOA-D1, (d) QViT-QAOA-D2 .

In figure 4.3, the classification report analysis indicates that, QViT-QAOA-D1 and QViT-QAOA-D2 have symmetrical performance, and all metrics are greater than 0.96 on each class. By comparison, the Basic VQC variants are more inconsistent with the QViT-Basic-D1 returning a very low precision value on crime free cases (0.95), and QViT-Basic-D2

having decreased malignancy classification performance (0.95 precision, 0.96 recall). All settings show near-perfect results on normal tissue classification (>0.99 in all metrics) affirming effective quantum feature distinction in normal tissue classification. The malignant group will continue to be the most difficult of them all but the QAOA versions perform in an almost unvaried equilibrium (0.97 to 0.99) against the Basic VQC renditions which displayed a greater range (0.95 to 0.98).

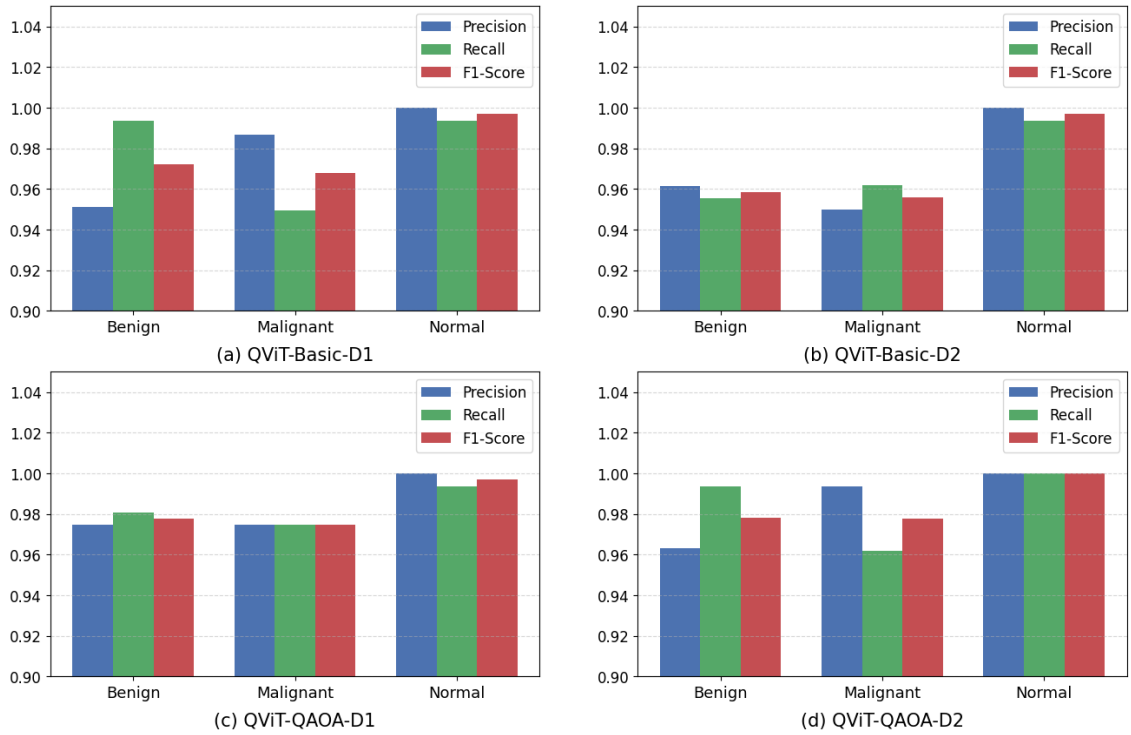

Figure 4.3. The classification report over three classes (Benign, Malignant, Normal) of four QViT configuration (a) QViT-Basic-D1, (b) QViT-Basic-D2, (c) (d) QViT-QAOA-D1, (d) QViT-QAOA-D2.

ROC curves of figure 4.4, establish strong medical-scientific potential of all QViT configurations with close to maximal AUC scores of close to unit, each cancer type. QViT-QAOA-D1 outperforms by providing highest AUC scores of 0.997, 0.998, and 1.000 respectively out of benign, malignant and normal classification whereas QViT-QAOA-D2 also demonstrates comparable results with AUC values as 0.998, 0.997 and 1.000 respectively. Simple VQC models portray a slightly lower, though impressive AUC range of above 0.995 on all categories with QViT-Basic-D1 and QViT-Basic-D2. Both the

configurations resulted in optimal discrimination between normal tissues (AUC = 1.000) indicating strong performance in quantum feature feature extraction of healthy tissues. The curves depict a typical upward steep slope to the upper left corner with a low and almost flat false positive rates at any of the operating points indicating a high sensitivity-specificity trade-off desirable in clinical diagnostic test applications.

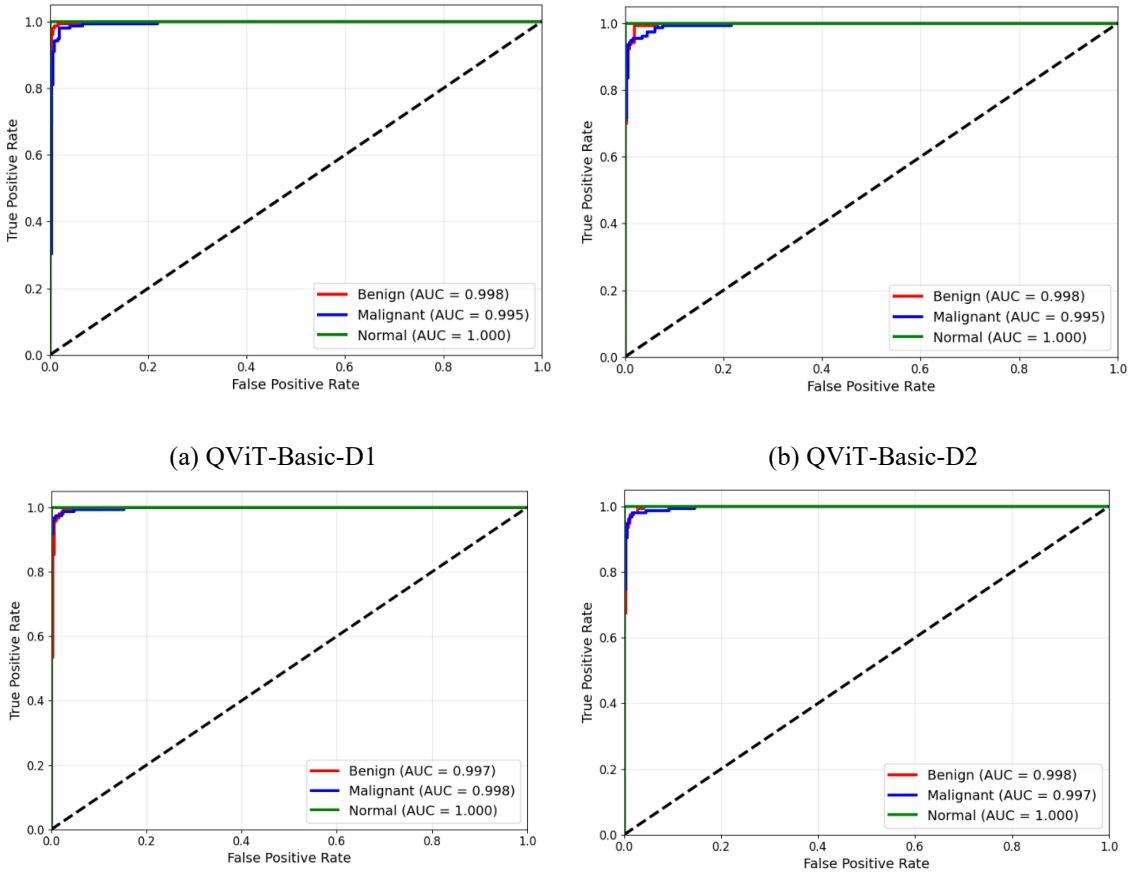

(a) QViT-Basic-D1

(b) QViT-Basic-D2

(c) QViT-QAOA-D1

(d) QViT-QAOA-D2

Figure 4.4. The ROC curve and AUC score over three classes (Benign, Malignant, Normal) of four QViT configuration (a) QViT-Basic-D1, (b) QViT-Basic-D2, (c) (d) QViT-QAOA-D1, (d) QViT-QAOA-D2.

4.2.2 Results of Quantum State Tomography

This subsection demonstrates the results of a Quantum State Tomography (QST) comparison of QViT the model around two different quantum processing elements. The four architectures examined in the dual-scale analysis are (i) QViT-QAOA-D1, (ii) QViT-QAOA-D2, (iii) QViT-Basic-D1, and (iv) QViT-Basic-D2, and the reason QViT takes a heterogeneous approach to quantum circuits is that we compare their performance on quantum multi-head attention using 12-qubit scale and quantum feed-forward networks using 8-qubit scale. The results of both depolarizing noise free and 1 % depolarizing noise conditions were examined against the theoretical potential and short-term hardware performance. This particular analysis is based upon the factors of gate efficiency, entanglement overhead, depth barrier and NISQ deployment feasibility in deciding the most practical QViT quantum circuit design.

4.2.2.1 Circuit-Level Architectural Analysis

The table below compares quantum circuit architectures of QViT variants, and a ranking of compatibility with NISQ based on the number of standard gates as might be required in an existing implementation [10, 13, 45, 48]. Demonstrating a range of levels of complexity, Basic-D1 does not demand significant amounts of resources, whereas Basic-D2 demands dramatically more. The gate efficiency of AOA architectures compares favorably with that of CNOT based architectures with typically minimum CNOTs and reasonable total gate counts. Analysis of circuit depths shows that QAOA has outstanding performance at its shallow depths (5-7) as compared to those of Basic VQC (15-28). The NISQ rankings show that QAOA-D1 has the best performance (rank 1 both on 12 qubits and 8 qubits) and Basic-D2 has the worst (rank 4, 12 qubits; rank 3, 8 qubits) performance because of the large number of CNOT gates and an inability to meet the depth constraint. The comparison shows that QAOA architectures value gate efficiency and shallow circuits, with Basic VQC architectures making the tradeoff of hardware efficiency in favor of the (possibly) greater quantum expressivity of dense connectivity patterns.

Table 4.2: Quantum Circuit Architecture Comparison for QViT Configurations on 12 qubit (Quantum Multi-Head Attention) and 8 qubit (Quantum Feed-Forward Network) for experimented single transformer block.

Qubit	Configuration	Total Gates	CNOTs	Circuit Depth	NISQ Ranking
12 qubit	QViT-Basic-D1	36	12	15	2
	QViT-Basic-D2	60	24	28	4
	QViT-QAOA-D1	42	6	5	1
	QViT-QAOA-D2	66	6	7	3
8 qubit	QViT-Basic-D1	24	8	15	2
	QViT-Basic-D2	40	16	28	3
	QViT-QAOA-D1	28	4	5	1
	QViT-QAOA-D2	44	4	7	2

4.2.2.2 Quantum State Properties via Tomography

Figure 4.5 tabulates the quantum state characteristics 12-qubit VQC setups in multi-head attention in the conditions without noise and with 1 percent of noise. Figure 4.5(a) reveals that Basic-D1 builds a base of mixed quantum states with medium reconstruction fidelity (0.383-0.403), entropy (1.440-1.627), and entanglement (1.402-1.587) that reflects a balanced quantum complexity. Figure 4.5(b) indicates that optimization of quantum cast over enhanced quantum expressivity specifically increases entropy (2.842- 2.875) and entanglement (1.899-1.953) and better fidelity (0.673-0.683) with the superior reconstruction accuracy (trace distance 0.134 -0.191) for adequate exploration of quantum state spaces. Figure 4.5(c) shows that QAOA-D1 favors quantum coherence keeping its states high purity (0.981-1.000) with minimal entropy (~0.000-0.113) and little entanglement (~0.000-0.076), but again has reconstruction challenges (trace distance 0.751-0.899). Figure 4.5(d) demonstrates the contingent performance of QAOA-D2 with

weakening fidelity (0.074-0.095) and serious span problems (trace distance 0.929-0.973) but keeping the typical pure-state pattern. Figure 4.5(e) reveals the inherent architectural split in terms of tomographic reconstruction with Basic setups leading to lower reconstruction errors than the high reconstruction errors found in QAOA. Fig. 4.5(f) shows very high values of quantum Fisher information, with QAOA-D2 providing the best parametrization sensitivity (3.643 noiseless, 3.602 with 1% noise), followed by QAOA-D1 (2.723 noiseless, 2.693 with 1% noise), indicating that QAOA algorithms do possess genuine quantum advantages in the parameter estimation problem as well as in comparable computational tasks.

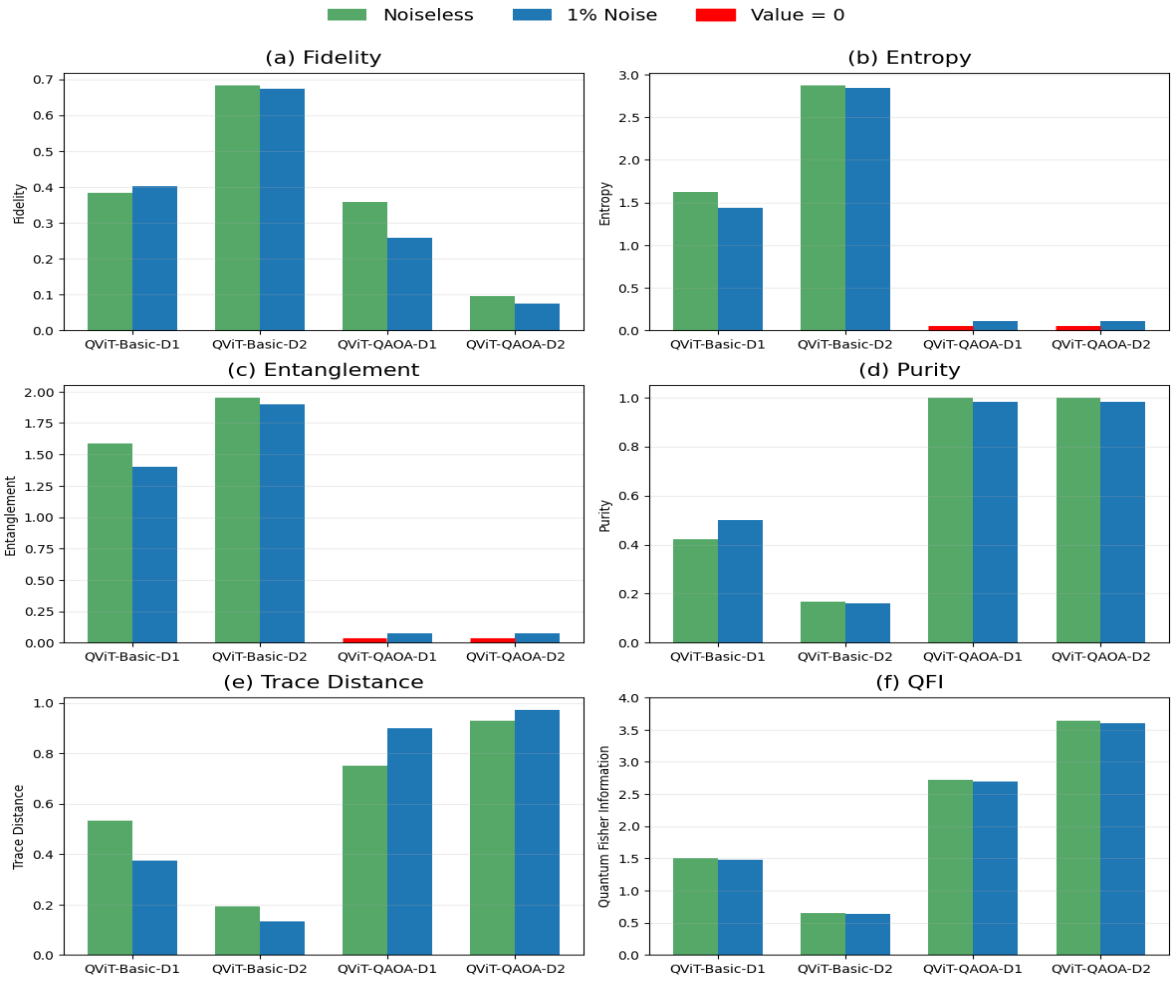

Figure 4.5: Quantum state properties of 12-qubit variational quantum circuits in quantum multi-head attention architectures under noiseless and 1% depolarizing noise conditions.

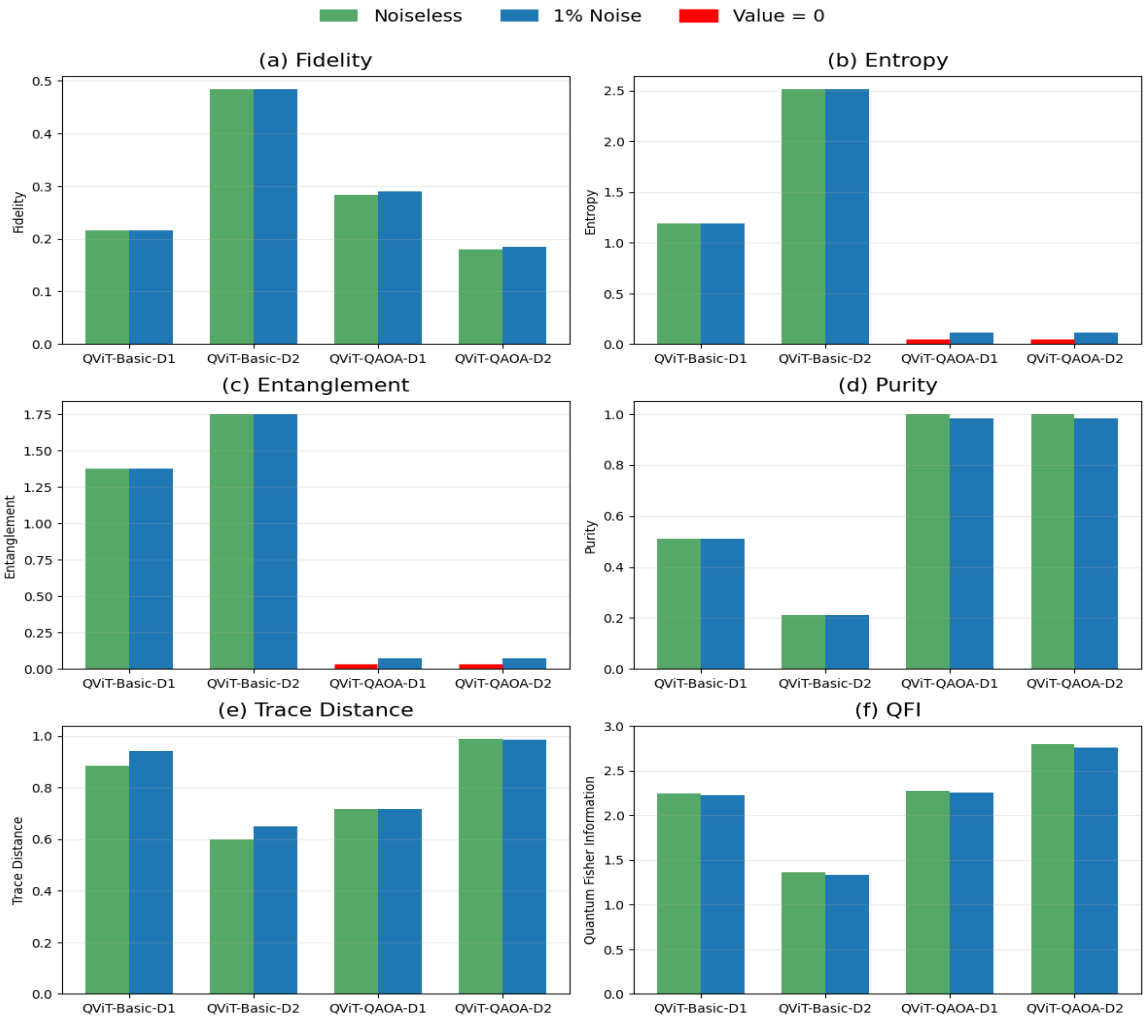

Figure 4.6: Quantum state properties of 8-qubit variational quantum circuits in quantum feed-forward network architectures under noiseless and 1% depolarizing noise conditions.

Figure 4.6 shows the properties of 8-qubit VQC circuit structures in feedforward networks. The figure 4.6(a) defines Basic-D1 with balanced quantum features of moderate fidelity (0.216), entropy (1.192), entanglement (1.374), and purity (0.511), but with higher trace distance (0.883-0.940). Figure 4.6(b) illustrates a spectacular quantum complexity increase of Basic-D2, doubling entropy (2.515), huge entanglement (1.753), increased fidelity (0.484), and better reconstruction (trace distance 0.598-0.648). Figure 4.6(c) and Figure 14(d) shows that QAOA maintains sharp states well across depths (purity 0.981-1.000) with little entanglement (0.000-0.076) and minimal entropy (0.000-0.113), though with

performance limitations in scaling to more qubits due to low fidelity (0.179-0.289) and poor reconstruction quality (trace distance 0.715-0.989). The quantitative performance gap shown in Figure 4.6(e) indicates that the Basic configurations are more efficient than the QAOA in terms of quantum state reconstruction quite generally, including possible tomographic issues in the QAOA. Figure 4.6(f) supports the significant quantum Fisher information within the configurations, where the ranges are (1.331-2.250), which implies the ability to measure a parameter (1.331-2.250) times sensitivity with respect to circuits observing computational capabilities.

All in all, the QST analysis shows the presence of unique quantum states properties across four configurations and that QViT-QAOA-D1 is the most promising in terms of exploiting quantum benefits. QViT-QAOA-D1 has the most desirable combination of quantum features: it encodes states with high purity (0.981-1.000), which enable them to remain in the quantum coherent regime in the presence of noise, and to a high degree of parameter sensitivity [QFI: 2.723] in both computer and sensing contexts. QViT-Basic-D2 supports the best quantum expressivity with maximum generation of entanglement (1.953) and entropy (2.875), which marks the greatest form of quantum computational advantage, but at a cost of the need to train deeper circuits that could undermine quantum coherence in the NISQ era. QViT-QAOA-D2 used in quantum sensing achieves the best parameter sensitivity (QFI: 3. 643), with the poorest quantum state reconstruction. The balanced quantum characteristic of QViT-Basic-D1 is characterized by a large degree of entanglement (1.587) and parameter sensitivity (QFI: 1.502). The inherent tradeoff between quantum expressibility and coherence retention supports the path chosen by QAOA-D1 where in-depth quantum state purity is valued to emulate quantum superiority under practical hardware limitations and offer enough quantum aid across a variety of quantum information processing applications. This makes QViT-QAOA-D1 the most promising solution to achieve long-termed quantum advantages in settings where quantum computing will have practical application.

4.2.3 Bayesian Hyperparameter Optimization for QViT-QAOA-D1

With the QViT-QAOA-D1 architecture, the model performed well with diagnosis in lung cancer classification achieving 99.30% AUC and 98.52% accuracy when using default hyperparameters. Importantly, this was performed on a shallow setup of 70 gates, which is both friendly to near-term NISQ systems. QViT-QAOA-D1 showed a superior balance amongst diagnostic performance, circuit complexity, and sparsity with respect to noise, suggesting it to be the best overall candidate to optimize using Bayesian hyperparameter optimization.

Table 4.3: Bayesian Optimization trial results (10 trials).

Trial	AUC	Accuracy	Precision	Recall	F1-Score	Status	Duration (min)
0	0.9975	0.9767	0.9778	0.9767	0.9767	Completed	24.2
1	0.9986	0.9789	0.9790	0.9789	0.9789	Completed	30.5
2	0.9983	0.9899	0.9899	0.9899	0.9899	Completed	37.2
3	0.9989	0.9931	0.9934	0.9931	0.9931	Completed	34.8
4	-	-	-	-	-	Pruned (OOM)	-
5	0.9976	0.9704	0.9707	0.9704	0.9704	Completed	24.9
6-9	-	-	-	-	-	Pruned (OOM)	-

Bayesian optimization was used to refine the seven most important hyperparameters of QViT including patch size, hidden size, number of attention heads, number of transformer blocks, MLP hidden size, learning rate, and a dropout rate (Table 3.1). This was carried out to optimize model capacity, expressivity of attention, depth of network and regularization and stabilize convergence. Ten trials were run, six of them successfully completed and four were pruned as a result of OOM errors. According to Table 4.3, Trial

3 had the best accuracy of 99.31% and AUC of 0.9989, precision of 99.34%, recall 99.31%, and F1-score of 99.31%, and serviced in a duration of 34.8 minutes. Trial 1 showed an almost identical AUC when compared with Trial 5 (0.9986), with slightly lower accuracy, whereas Trial 5 had the lowest run time (24.9 minutes), but a lower accuracy of 97.04 percent. These findings exemplify the trade-off between training efficiency and predictive performance, of which Trial 3 offered the most successful balance with 50% accuracy in the predictive performance and an efficiency rate of 0.39 during training process.

Table 4.4: Hyperparameter configuration of before applying (Pre) Bayesian Hyperparameter Optimization and best trial Configuration (Trial 3) after applying (Post) Bayesian Hyperparameter Optimization for QViT-QAOA-D1 configuration.

Parameter Name	**Pre Optimization**	**Post Optimization**	**Architectural Impact**
Patch size	128	128	Unchanged
Hidden size	12	4	Reduced quantum attention dimensionality
Number of heads	2	4	Increased attention parallelism
Transformer blocks	1	1	Unchanged
MLP hidden size	8	16	Doubled quantum MLP capacity
Learning rate	Warmup Cosine Decay Schedule	0.003718	Simplified optimization
Dropout rate	0.1	0.1	Unchanged

In table 4.4, the top configuration of Trial 3 showed relatively large architectural changes with Bayesian optimization. The hidden size was scaled downwards by a factor of 3 (contracting quantum attention to 4 qubits, doubling attention heads to 4 and expanding MLP hidden size by a factor of 2 to 16 qubits). It was learned rate changing to 0.003718.

This is a key architectural redesign as opposed to hyper parameter optimization The quantum attention mechanism now works with 4-dimensional features that have been compressed on 4 heads, whereas quantum MLP works on expanded 16-dimensional representations. Optimization analysis found that focused quantum mixture in feed-forward networks have a better potential than distributed quantum attention strategy in the original architecture. As shown in table 4.5, the performance was improved significantly: the AUC was advanced by 0.59 percent (0.9930 to 0.9989) and accuracy by 0.79 percent (98.52 to 99.31). Although total gate count is still 70, this is full architectural redistribution of 12-qubit attention (42 gates) + 8-qubit MLP (28 gates) into 4-qubit attention (14 gates) and 16-qubit MLP (56 gates).

Table 4.5. Pre vs Post-Optimization performance results of QViT-QAOA-D1 configuration.

Metric	**Pre-Optimization Results**	**Post-Optimization Results**	**Improvement**
AUC	0.9930	0.9989	+0.59%
Accuracy	98.52%	99.31%	+0.79%
Gate Complexity	70 gates (42 gates [12 qubit] 28 gates [8 qubit])	70 gates (14 gates [4 qubit] 56 gates [16 qubit])	Reconfigured

These results demonstrate the value of systematic hyperparameter optimization in discovering effective quantum resource allocation for vision transformers, showing that initial parameter choices can be significantly improved through principled optimization methods.

4.2.4 NISQ level Noise Resilience Analysis for QViT-QAOA-D1 configuration

Because QViT-QAOA-D1 demonstrated the best lung cancer classification accuracy, the next concern was whether its high accuracy could hold up in the face of noisy quantum hardware. Existing NISQ-based devices are subject to decoherence, gate error, and measurement noise that present a risk to both diagnostic and quantum fidelity. To verify this, we performed a noise resilience study with realistic operating conditions, to test the

robustness of QViT-QAOA-D1. The findings indicate that the model results in high predictive reliability and the model is compatible with NISQ.

Table 4.6 shows the cumulative assessment of the QViT-QAOA-D1 in realistic NISQ noise environments of 0.0% to 2.0%. The model has high robustness with robustness performance rating of more than 98.5% on lung cancer classification across the levels of noise settings. AUC scores of the model are extremely high (0.992-0.994), and there is minimal degradation even at the most severe 2.0% noise level, where the model still has 0.993 retention with an AUC of 0.994+/- 0.000. The slightest changes occur in Accuracy and F1-Score, which also demonstrate the stability of the circuit concerning decoherence and gate errors. These results show that QViT-QAOA-D1 retains quantum-enhanced diagnostic potential in the context of the current NISQ hardware limitations.

Table 4.6: Noise resilience evaluation of QViT-QAOA-D1 for lung cancer classification on NISQ Systems.

Noise Level	**Noise Rate**	**Seed (n)**	**AUC (Mean±SD)**	**Accuracy (Mean±SD)**	**F1-Score (Mean±SD)**	**Retention (%)**
Ideal	0.0%	3	0.992±0.002	0.961±0.004	0.961±0.004	100.0
Low-1	0.3%	3	0.994±0.001	0.958±0.002	0.958±0.002	99.7
Low-2	0.5%	3	0.994±0.002	0.957±0.015	0.957±0.015	99.6
Medium-1	0.8%	3	0.993±0.002	0.947±0.008	0.947±0.008	98.5
Medium-2	1.0%	3	0.994±0.002	0.956±0.002	0.956±0.002	99.5
High-1	1.5%	3	0.994±0.002	0.956±0.006	0.956±0.006	99.5
High-2	2.0%	3	0.994±0.000	0.954±0.004	0.954±0.004	99.3

Table 4.7 shows individual-seed performance of QViT-QAOA-D1 across all noise levels simulated, which shows resistance even to stochastic quantum noise. Three independent runs (42, 142, 242) provide consistent quantum advantages and significant improvements with only slight deviations, which fall within clinically acceptable margins (± 2-3%

accuracy). Among the seeds, 142 also has the most durable performance, with peak accuracy of 97.04% at 0.5% noise, whereas seed 242 is the more easily perturbed, falling by 0.21 to 95.98% at 2.0%. Notably, the F1-scores are strictly kept between 0.947 and 0.961 in all condition due to the balanced sensitivity-specificity trade-off requirement to perform reliable diagnosis of lung cancer.

Table 4.7: Individual seed performance across all noise levels.

Seed	AUC score	Accuracy	F1-score
Ideal (0.0% Noise)			
42	0.9909	0.9556	0.9556
142	0.9949	0.9641	0.9641
242	0.9916	0.9619	0.9619
Low-1 (0.3% Noise)			
42	0.9949	0.9556	0.9556
142	0.9943	0.9577	0.9577
242	0.9934	0.9598	0.9598
Low-2 (0.5% Noise)			
42	0.9945	0.9641	0.9641
142	0.9954	0.9704	0.9704
242	0.9909	0.9366	0.9366
Medium-1 (0.8% Noise)			
42	0.9945	0.9535	0.9535
142	0.9946	0.9514	0.9514
242	0.9898	0.9366	0.9366

Seed	AUC score	Accuracy	F1-score
Medium-2 (1.0% Noise)			
42	0.9947	0.9535	0.9535
142	0.9958	0.9577	0.9577
242	0.9917	0.9556	0.9556
High-1 (1.5% Noise)			
42	0.9952	0.9577	0.9577
142	0.9948	0.9619	0.9620
242	0.9908	0.9471	0.9472
High-2 (2.0% Noise)			
42	0.9936	0.9493	0.9493
142	0.9938	0.9535	0.9535
242	0.9935	0.9598	0.9598

4.2.5 Performance comparison with existing studies

Table 4.8 compares QViT with some related quantum machine learning methods on a range of medical imaging classifications. On the rather large dataset of 3,150 CT images, the proposed QViT has an accuracy of 98.52 in detecting lung cancer, beating other several existing models. As an example, a 99.25% accuracy coefficient was obtained by Bilal et al. IQI-BGWO-SVM only on 332 breast cancer locations, whereas BC-QNet finished at 96.54-98.01% with 322 samples. Mahmood et al. experimented to attain the best accuracy of 98.9 on breast pathology in a 2,000 images dataset which is relatively smaller in size as compared to QViT. In lung cancer, specifically, Radhika & Sharada achieve 97% accuracy

with 1,018 images but training time consuming 5.4 hours, whereas QViT used 13 times faster training time (two hours) and improved accuracy by 1.3 percent. QViT also outperformed Bilal et al.'s Q-GBGWO-ELM (96.98% accuracy on 910 images with lung cancer) as it recorded higher accuracy on 3.6 times more data points. In other modalities, Hussein et al. 89.3 in skin cancer with long runtimes, Ticku et al. 92.13 in brain tumors, and Muniasamy et al. 94 in brain tumors. The quality of consistency and accuracy is particularly good with QViT. In general, the analysis of the datasets indicates that current studies present powerful findings, but largely select highly specific or small scale data. Compared to QViT, however, QViT shows not only clinical robustness but also greater computational efficiency, maintaining high accuracy in a larger and more heterogeneous dataset, making it look like a better candidate to be used in real medical practice.

Table 4.8. Comparison of the QViT models' performance with existing literature.

Author	**Model Name**	**Application (image type)**	**No. of images in dataset**	**Accuracy**	**Training Time**
Bilal et al. [36]	IQI-BGWO-SVM	Breast Cancer (Mammographic)	332 images	99.25 %	Not mentioned
Bilal et al. [48]	BC-QNet	Breast Cancer (Mammographic)	322 images (MIAS dataset),	97.24 % (Benign), 98.01 % (Malignant), 96.54 % (Normal)	Not mentioned
Mahmood et al. [28]	MFF-HistoNet (CNN+QTN)	Breast Cancer (Tissue pathology)	2082 images (100 × magnification), 1995 images (40 × magnification)	98.8% (100 × magnification), 98.9% (40 × magnification)	Not mentioned

Author	Model Name	Application (image type)	No. of images in dataset	Accuracy	Training Time
Hussein et al. [12]	HQCNN-BiLSTM-MobileNetV2	Skin Cancer	2637 images	89.3%	2981 seconds
Radhika & Sharada [26]	QHO-CNN	Lung Cancer (CT scan)	1018 images	97%	5.431 hours
Bilal et al. [11]	Q-GBGWO-ELM	Breast Cancer (Mammographic), Brain Tumor (MRI scan), Skin Cancer (Dermoscopic), Lung Cancer (CT scan)	322 images (BC), 2000 images (SC), 910 images (LC), 3064 images (BT)	98.80% (BC), 97.00% (SC), 96.98% (LC), 92.30% (BT)	Not mentioned
Ticku et al. [29]	QCNN	Brain Tumor (MRI scans)	3064 images	92.13%	1.1 seconds per image training
Muniasamy et al. [38]	HQC-CNN	Brain Tumor (MRI scans)	3064 images	94%	Not mentioned
Ours	**QViT (QViT-QAOA-D1 configuration)**	**Lung Cancer (CT Scan)**	**3150**	**98.52 %**	**674.93 seconds**

4.2.6 Performance comparison with state-of-the-art models

A comparison between the proposed QViT model and the other state-of-the-art deep learning architectures is given in Table 4.9. As it can be seen, the highest accuracy (98.52%) was reached by QViT-QAOA-D1, whose precision, recall, and F1-score were 98%. This result is close to what was obtained by DenseNet201 (98.32%) and ConvNeXtBase (98.10%) but QViT exhibits a decided superiority in model efficiency with only 196987 parameters as compared to tens of millions of parameters in the previous classical networks. Although MobileNetV3Large has the lowest number of parameters, the model had less than 50 percent accuracy. Compared to this, QViT does not incur a large parameter cost and still reaches a state-of-the-art accuracy, demonstrating its scalability and utility to medical imaging problems.

Table 4.9: Comparison of the QViT models' performance with state-of-the-art models.

Model Name	**Error Rate (%)**	**Precision (%)**	**Recall (%)**	**F1-score (%)**	**Accuracy (%)**	**No. of Parameters**
Vision Transformer	0.29	94	93	93	94.33	4,080,074
Swin Transformer	0.16	97	97	97	97.02	86,459
DenseNet201	0.08	98	98	98	98.32	18,321,984
ResNet152V2	0.14	97	97	97	97.04	58,331,648
InceptionV3	0.50	89	89	89	89.43	21,802,784
MobileNetV3Large	2.4	49	49	49	49.26	2,996,352
ConvNeXtBase	0.9	98	98	98	98.10	87,566,464
QViT (QViT-QAOA-D1)	**0.9**	**98**	**98**	**98**	**98.52**	**196,987**

4.3 Discussion

This research shows that quantum-enhanced vision transformers can help to connect the theoretical quantum computational superiority and practical medical imaging work. The quantum state tomography analysis indicates that Basic VQC settings have better quantum expressivity by way of greater entanglement entropy (1.899-1.953) and greater state complexity, permitting quantum circuits to represent more subtle correlations in CT scan data than may be used by classical transformers. The quantum advantage scales to greater circuit depths (15-28), though, which demands more gates and, in the small scale, is impractical as NISQ. In contrast, QAOA-based circuits do not emphasize some degree of quantum coherence preservation (0.981-1.000) or low decoherence, thus much more readily deployable on existing quantum devices, without significant quantum benefit losses. The results of the classification show that the quantum enhancement leads to actual diagnostic improvement with QViT-QAOA-D1 performing on 98.52 percent accuracy with 42 gates in quantum attention and 28 gates in quantum MLP with single transformer block. The high performance in malignant versus benign classification (AUC >0.997) shows that quantum circuits have a better feature discrimination power essential in medical diagnosis. The resilience tests of the noise show that quantum benefits can be used under realistic hardware constraints, as model performance can be maintained above > 98.5 percent at all noise levels (0.0%-2.0%) and thus quantum-enhanced medical imaging can work effectively on NISQ devices. The Bayesian optimization findings demonstrate that quantum-classical hybrid structures can be optimized methodically to be used in clinical applications and use a 0.79 percent improvement, and exhibit the same quantum circuit complexity. The comparative analysis also illustrates that QViT has found the right balance to the quantum advantage vs practical deployment trade-off with scalability (3,150 images) along with an efficiency (674 seconds training time) important to the clinical acceptance of the tool. These results are supported by the QFI analysis that shows real parameter sensitivity potentials in all configurations with QAOA-D2 being the most sensitive and QAOA-D1 the most sensible tradeoff between parameter sensitivity and hardware compatibility. These observations point to the possibility of practical quantum machine

learning being the task of meeting the desired quantum enhancement level as limiting additional realistic constraints as opposed to the maximization of theoretical quantum benefits. The QAOA-inspired method shows that problem-specific quantum circuit design can lead to not only quantum computational advantages, but also to parameter sensitivity as a means of sensing, and compatibility with near-term hardware, creating a path toward quantum advantage in real-world traditionally non-quantum artificial intelligence systems.

CHAPTER 5
IMPACT ON SOCIETY, ENVIRONMENT AND SUSTAINABILITY

5.1 Impact on society

The QViT proposed framework is highly socially relevant because it allows the accuracy and efficiency of lung cancer diagnoses to be increased. Early and accurate diagnosis leads to early improvement in patient status, the reduction of treatment costs, and associated load on the healthcare system. The research also leads to innovation in digital healthcare as by combining high level AI with developing quantum technologies, it would create a pathway to more available diagnostic support in resource poor areas. In addition, the work could be used in academic and industrial developments of quantum machine learning and, in future, interactions with clinicians, researchers, and technologists could be introduced to solve global health problems by means of interdisciplinary solutions.

5.2 Impact on the environment

Environmentally, this study focuses on resource efficient computation of the required resources. Conventional deep learning algorithms typically have high parameter count and energy consumptions that lead to a high carbon-footprint. You can also notice that QViT shows competitive accuracy using much fewer parameters thus being energy aware of model design. Smaller and optimized circuits are also the means of achieving lower hardware overhead when experimentation is done. Enabling more lightweight architectures which are compatible with NISQ components, the work helps to create a more sustainable mindset in medical AI research. Therefore, the project achieves not only improved patient care, but also squares itself with ongoing initiatives to decrease the energy load in computing.

5.3 Ethical Aspects

Ethical factors will be of crucial significance in the implementation of AI-based medical systems. In this study, confidentiality and privacy of the patient are respected, as only data were anonymized and used to fulfill academic intentions. QViT designs underlines fairness by assessing the performance over balanced datasets, thus limiting the risks of bias in clinical performance. Moreover, the explanation of model judgments by verifying quantum states increases the model transparency so that clinicians could trust AI results. The research also appreciates the duty of the researchers in deterring abuse of sensitive medical AI technologies. Ethical rigor in general contributes to the validity and the social acceptability of the proposed framework.

5.4 Sustainability Plan

The longevity of this study is that it can be contextualized with changing technology and health demands. The framework is developed by using NISQ-compatible architectures and, thus, can be executed on existing hardware as well as in a scalable manner on future fault-tolerant quantum systems. The parameterization of QViT is of light-weight, hence is efficient in the long run, which is desirable in the deployment environment where resources are limited, such as hospitals and diagnostic centers. Moreover, openly publishing academic results helps to promote subsequent and future replications as well as extensions by other researchers, and is thus wellspring of impact. The long-term goal of the described work is to develop a framework capable of supporting effective clinical applications of quantum-assisted medical AI that considers clinical applicability, computation and resource constraints, and social value.

CHAPTER 6
CONCLUSION AND FUTURE WORK

6.1 Summary of the Study

The study presented a Quantum enhanced Vision Transformer (QViT) to classify lung cancer as it introduced variational quantum circuits (VQCs) as enhancements of the attention and feed-forward layers by improving feature learning. The two circuit families of Basic VQC and QAOA were examined at various depths, which yields four sets. An experiment on 3,150 CT images indicated that QViT-QAOA suffered the least accuracy with 98.52%, despite a large reduction in parameters relative to state-of-the-art models. Quantum state tomography (QST) verified the presence of genuine quantum contributions and noise simulations verified that the method was robust to NISQ limitations. The outcomes indicate that QViT is an efficient, scalable and clinically-relevant solution to quantum-assisted medical imaging.

6.2 Conclusions

This paper shows that quantum-enhanced Transformers offer a promising direction towards the future improvements in the medical image analysis while being practical and constrained to near-term quantum hardware. The QViT architecture forms a promising step towards providing a useful co-design of quantum comp advantages in classical transformer architecture, and could eventually apply to quantum-enhanced differences in other fields. This contribution establishes the validity of authentic quantum contributions to medical imaging applications back using the processes of systematic quantum state tomography and noise resilience analysis. The QAOA-inspired method comes out as the best tradeoff between quantum expressivity and hardware feasibility, with shallow circuit implementations possible to be deployed on NISQ. These results set a path toward quantum-enhanced vision transformers as a potential base of clinical AI, providing both an opportunity to harness the theoretical quantum-enhanced speed in practical settings and harness the diagnostic demands in clinical applications.

6.3 Implication for Further Study

These results indicate a few key areas of development of quantum-enhanced medical imaging. Although the proposed QViT framework performed well on 3,150 CT image samples, future study should test its scalability at high scale, such as 10,000+ samples, where quantum machine learning algorithms tend to register barren plateau effects and trainability issues. Even the present practice of 4-qubit subsystem tomography restricted our visibility of multi-qubit correlations, which makes it desirable to have new techniques of quantum state characterization as process tomography and compressed sensing. Also, simulations were done on environments with limited available computing resources, which do not completely represent what the hardware experience offers in terms of decoherence, crosstalk, and calibration problems. Translating the algorithm to hardware on a physical device e.g. IBM Quantum, Google Quantum AI, or IonQ is thus a significant development step to validate practical viability. In addition to scalability and hardware testing, generalizing QViT to include multi-modal medical images such as MRI, ultrasound, and X-ray imaging, may help lead to more generalizability. One route to faster deployment would be to explore new forms of circuit architecture beyond Basic VQC and QAOA, and integration of quantum federated learning strategies or co-design approaches, especially in collaborative healthcare settings. Together, the details provided will assist in putting typical standards in place and lead the way to clinically applicable quantum-assisted diagnostics.

REFERENCES

[1] Nicholson, A. G., Tsao, M. S., Beasley, M. B., Borczuk, A. C., Brambilla, E., Cooper, W. A., ... & Travis, W. D. (2022). The 2021 WHO classification of lung tumors: impact of advances since 2015. Journal of Thoracic Oncology, 17(3), 362-387.

[2] Li, M., Ma, X., Chen, C., Yuan, Y., Zhang, S., Yan, Z., ... & Ma, M. (2021). Research on the auxiliary classification and diagnosis of lung cancer subtypes based on histopathological images. Ieee Access, 9, 53687-53707.

[3] Pandey, S. K., & Bhandari, A. K. (2023). A systematic review of modern approaches in healthcare systems for lung cancer detection and classification. Archives of Computational Methods in Engineering, 30(7), 4359-4378.

[4] Sasaki, T., Kuno, H., Hiyama, T., Oda, S., Masuoka, S., Miyasaka, Y., ... & Kobayashi, T. (2024). 2021 WHO classification of lung cancer: molecular biology research and radiologic-pathologic correlation. Radiographics, 44(3), e230136.

[5] Friedman, J. R., Patel, V., Chen, W., Tolpygo, S. K., & Lukens, J. E. (2000). Quantum superposition of distinct macroscopic states. nature, 406(6791), 43-46.

[6] Horodecki, R., Horodecki, P., Horodecki, M., & Horodecki, K. (2009). Quantum entanglement. Reviews of modern physics, 81(2), 865-942.

[7] Biamonte, J., Wittek, P., Pancotti, N., Rebentrost, P., Wiebe, N., & Lloyd, S. (2017). Quantum machine learning. Nature, 549(7671), 195-202.

[8] Havlíček, V., Córcoles, A. D., Temme, K., Harrow, A. W., Kandala, A., Chow, J. M., & Gambetta, J. M. (2019). Supervised learning with quantum-enhanced feature spaces. Nature, 567(7747), 209-212.

[9] Zhou, L., Wang, S. T., Choi, S., Pichler, H., & Lukin, M. D. (2020). Quantum approximate optimization algorithm: Performance, mechanism, and implementation on near-term devices. Physical Review X, 10(2), 021067.

[10] Cerezo, M., Arrasmith, A., Babbush, R., Benjamin, S. C., Endo, S., Fujii, K., ... & Coles, P. J. (2021). Variational quantum algorithms. Nature Reviews Physics, 3(9), 625-644.

[11] Bilal, A., Shafiq, M., Obidallah, W. J., Alduraywish, Y. A., & Long, H. (2025). Quantum computational infusion in extreme learning machines for early multi-cancer detection. Journal of Big Data, 12(1), 1-48.

[12] Hussein, A. A., Montaser, A. M., & Elsayed, H. A. (2025). Skin cancer image classification using hybrid quantum deep learning model with BiLSTM and MobileNetV2. Quantum Machine Intelligence, 7(2), 1-28.

[13] Bharti, K., Cervera-Lierta, A., Kyaw, T. H., Haug, T., Alperin-Lea, S., Anand, A., ... & Aspuru-Guzik, A. (2022). Noisy intermediate-scale quantum algorithms. Reviews of Modern Physics, 94(1), 015004.

[14] Kandala, A., Mezzacapo, A., Temme, K., Takita, M., Brink, M., Chow, J. M., & Gambetta, J. M. (2017). Hardware-efficient variational quantum eigensolver for small molecules and quantum magnets. nature, 549(7671), 242-246.

[15] Azad, R., Kazerouni, A., Heidari, M., Aghdam, E. K., Molaei, A., Jia, Y., ... & Merhof, D. (2024). Advances in medical image analysis with vision transformers: a comprehensive review. Medical Image Analysis, 91, 103000.

[16] Li, J., Chen, J., Tang, Y., Wang, C., Landman, B. A., & Zhou, S. K. (2023). Transforming medical imaging with Transformers? A comparative review of key properties, current progresses, and future perspectives. Medical image analysis, 85, 102762.

[17] Takahashi, S., Sakaguchi, Y., Kouno, N., Takasawa, K., Ishizu, K., Akagi, Y., ... & Hamamoto, R. (2024). Comparison of vision transformers and convolutional neural networks in medical image analysis: A systematic review. Journal of Medical Systems, 48(1), 84.

[18] Aburass, S., Dorgham, O., Al Shaqsi, J., Abu Rumman, M., & Al-Kadi, O. (2025). Vision Transformers in Medical Imaging: a Comprehensive Review of Advancements and Applications Across Multiple Diseases. Journal of Imaging Informatics in Medicine, 1-44.

[19] Oviesi, S., & Tarokh, M. J. (2025). Quantum neural network-assisted learning for small medical datasets: a case study in emphysema detection. The Journal of Supercomputing, 81(1), 1-32.

[20] Tudisco, A., Volpe, D., & Turvani, G. (2025). Quantum Machine Learning in Healthcare: Evaluating QNN and QSVM Models. arXiv preprint arXiv:2505.20804.

[21] Saggi, M. K., Bhatia, A. S., Mensah, I. K., Gowher, H., & Kais, S. (2025). Multi-Omic and quantum machine learning integration for lung subtypes classification. Future Generation Computer Systems, 107905.

[22] Genç, S. (2025). Feature selection using quantum feature maps: Performance analysis of classical and quantum models on the breast cancer dataset. International Journal of Data Science and Applications, 8(1), 28-44.

[23] Hafidi, M. Y. E., Toufah, A., & Kadim, M. A. (2025). Investigating Quantum Feature Maps in Quantum Support Vector Machines for Lung Cancer Classification. arXiv preprint arXiv:2506.03272.

[24] Wei, L., Liu, H., Xu, J., Shi, L., Shan, Z., Zhao, B., & Gao, Y. (2023). Quantum machine learning in medical image analysis: A survey. Neurocomputing, 525, 42-53.

[25] Singh, L. K., Parida, P. K., & Guganathan, L. (2025, February). Detection of Lung Cancer in Histopathological Images Utilizing Self-Guided Quantum Generative Adversarial Network with Cat Hunting Optimization. In 2025 4th International Conference on Sentiment Analysis and Deep Learning (ICSADL) (pp. 693-699). IEEE.

[26] Radhika, S., & Sharada, G. (2025). Design and implementation of quantum hippo inspired convolutional neural networks using parametric quantum circuits for an efficient lung cancer classification. Discover Computing, 28(1), 1-18.

[27] Gangappa, M., Manju, D., Krishnna, M. G., Reddy, M. S. M., Sathish, M., Shahabaaz, S., ... & Chaitanya, M. (2025). Quantum-Enhanced Brain Tumor Detection and Progression Prediction Using MRI Imaging. Journal of Electronics, Electromedical Engineering, and Medical Informatics, 7(2), 493-507.

[28] Mahmood, T., Saba, T., & Rehman, A. (2025). Breast cancer diagnosis with MFF-HistoNet: a multi-modal feature fusion network integrating CNNs and quantum tensor networks. Journal of Big Data, 12(1), 60.

[29] Ticku, A., Sangwan, V., Balani, S., Jha, S., Rawat, S., Rathee, A., & Yadav, D. (2025). Advancing neuroimaging with quantum convolutional neural networks for brain tumor detection. International Journal of Information Technology, 1-8.

[30] Temme, K., Bravyi, S., & Gambetta, J. M. (2017). Error mitigation for short-depth quantum circuits. Physical review letters, 119(18), 180509.

[31] McArdle, S., Yuan, X., & Benjamin, S. (2019). Error-mitigated digital quantum simulation. Physical review letters, 122(18), 180501.

[32] Innan, N., Siddiqui, O. I., Arora, S., Ghosh, T., Koçak, Y. P., Paragas, D., ... & Bennai, M. (2024). Quantum state tomography using quantum machine learning. Quantum Machine Intelligence, 6(1), 28.

[33] Ma, H., Dong, D., Petersen, I. R., Huang, C. J., & Xiang, G. Y. (2024). Neural networks for quantum state tomography with constrained measurements. Quantum Information Processing, 23(9), 317.

[34] Quek, Y., Fort, S., & Ng, H. K. (2021). Adaptive quantum state tomography with neural networks. npj Quantum Information, 7(1), 105.

[35] Shinde, S. S., & Pande, A. (2025). High-Performance Computing-Based Brain Tumor Detection Using Parallel Quantum Dilated Convolutional Neural Network. NMR in Biomedicine, 38(6), e70035.

[36] Bilal, A., Imran, A., Baig, T. I., Liu, X., Abouel Nasr, E., & Long, H. (2024). Breast cancer diagnosis using support vector machine optimized by improved quantum inspired grey wolf optimization. Scientific Reports, 14(1), 10714.

[37] Scientific, L. L. (2025). A HYBRID QUANTUM-INSPIRED CNN ARCHITECTURE FOR EFFICIENT AND ACCURATE BRAIN TUMOR CLASSIFICATION WITH EXPLAINABILITY ANALYSIS. Journal of Theoretical and Applied Information Technology, 103(1).

[38] Muniasamy, A., Alquhtani, S. A., Alshehri, A. H., Begum, A., & Sabahath, A. (2025). Investigating Hybrid Quantum-Assisted Classical and Deep Learning Model for MRI Brain Tumor Classification. Journal of Image and Graphics, 13(1).

[39] Awujoola, J. O., Enem, T. A., Owolabi, J. A., Akusu, O. C., Abioye, O., AbidemiAwujoola, E., & OlayinkaAdelegan, R. (2025). Exploring the Intersection of Quantum Neural Networks and Classical Neural Networks for Early Cancer Identification. In Quantum Computing (pp. 147-169). Auerbach Publications.

[40] Frasca, M., Cutica, I., Pravettoni, G., & La Torre, D. (2025). Optimizing Melanoma Diagnosis: A Hybrid Deep Learning and Quantum Computing Approach for Enhanced Lesion Classification. Intelligence-Based Medicine, 100264.

[41] Rajamohana, S. P., Yelamali, V., Soni, P., Vanahalli, M., & Prasad, P. (2025). Hybrid Quantum Graph Neural Network for Brain Tumor MR Image Classification: HYBRID QUANTUM GRAPH NEURAL NETWORK FOR BRAIN TUMOR MR IMAGE. Journal of Scientific & Industrial Research (JSIR), 84(1), 60-71.

[42] Islam, M., Hasan, M. J., & Mahdy, M. R. C. (2025). CQ CNN: A Hybrid Classical Quantum Convolutional Neural Network for Alzheimer's Disease Detection Using Diffusion Generated and U Net Segmented 3D MRI. arXiv preprint arXiv:2503.02345.

[43] Katı, B. E., Küçüksille, E. U., & Sarıman, G. (2025). Enhancing Deepfake Detection Through Quantum Transfer Learning and Class-Attention Vision Transformer Architecture. Applied Sciences, 15(2), 525.

[44] Balasubramani, S., Renjith, P. N., Kavisankar, L., Rajavel, R., Malarvel, M., & Shankar, A. (2025). A Quantum-Enhanced Artificial Neural Network Model for Efficient Medical Image Compression. IEEE Access.

[45] Cross, A. W., Bishop, L. S., Sheldon, S., Nation, P. D., & Gambetta, J. M. (2019). Validating quantum computers using randomized model circuits. Physical Review A, 100(3), 032328.

[46] Arute, F., Arya, K., Babbush, R., Bacon, D., Bardin, J. C., Barends, R., ... & Martinis, J. M. (2019). Quantum supremacy using a programmable superconducting processor. Nature, 574(7779), 505-510.

[47] Monroe, C., Campbell, W. C., Duan, L. M., Gong, Z. X., Gorshkov, A. V., Hess, P. W., ... & Yao, N. Y. (2021). Programmable quantum simulations of spin systems with trapped ions. Reviews of Modern Physics, 93(2), 025001.

[48] Preskill, J. (2018). Quantum computing in the NISQ era and beyond. Quantum, 2, 79.

[49] Bilal, A., Imran, A., Liu, X., Liu, X., Ahmad, Z., Shafiq, M., ... & Long, H. (2024). BC-QNet: A quantum-infused ELM model for breast cancer diagnosis. Computers in biology and medicine, 175, 108483.

242-25-027

ORIGINALITY REPORT

5%	5%	2%	2%
SIMILARITY INDEX	INTERNET SOURCES	PUBLICATIONS	STUDENT PAPERS

PRIMARY SOURCES

1	dspace.daffodilvarsity.edu.bd:8080 Internet Source	2%
2	Submitted to Daffodil International University Student Paper	1%
3	data.mendeley.com Internet Source	<1%
4	"Interplay of Artificial General Intelligence with Quantum Computing", Springer Science and Business Media LLC, 2025 Publication	<1%
5	export.arxiv.org Internet Source	<1%
6	open.library.ubc.ca Internet Source	<1%
7	www.ijetsr.com Internet Source	<1%
8	peerj.com Internet Source	<1%